Journal of Structural Geology 160 (2022) 104621

Contents lists available at ScienceDirect

Journal of Structural Geology

journal homepage: www.elsevier.com/locate/jsg

The brittle evolution of Western Norway – A space-time model based on fault mineralizations, K–Ar fault gouge dating and paleostress analysis

Åse Hestnes [a,*], Deta Gasser [b,c], Thomas Scheiber [b], Joachim Jacobs [a], Roelant van der Lelij [c], Jasmin Schönenberger [c], Anna K. Ksienzyk [c]

[a] Department of Earth Science, University of Bergen, PB 7803, 5020, Bergen, Norway
[b] Department of Environmental Sciences, Western Norway University of Applied Sciences, Røyrgata 6, 6856, Sogndal, Norway
[c] Geological Survey of Norway, PB 6315, 7491, Trondheim, Norway

ARTICLE INFO

Keywords:
K-Ar fault gouge geochronology
Brittle deformation
Fault mineralization
Paleostress analysis
Western Norway

ABSTRACT

Basement fracture and fault patterns on passive continental margins control the onshore landscape and offshore distribution of sediment packages and fluid pathways. In this study, we decipher the spatial-temporal evolution of brittle faults and fractures in the northern section of the passive margin of Western Norway by combining field observations of fault mineralizations and K–Ar fault gouge dating with different paleostress approaches, resulting in the following model: (1) High-T fault mineralizations indicate Silurian NW-SE compression followed by NW-SE extension in the Early to Mid-Devonian. (2) Epidote, chlorite and quartz fault mineralizations indicate a dominant strike-slip stress field in the Late Devonian to early Carboniferous. (3) E-W extensional stress fields which could be related to Permo-Triassic or Late Jurassic rifting are not prominent in our data set. (4) K–Ar fault gouge ages indicate two extensive faulting events under a WNW-ESE transtensional stress regime with related precipitation of zeolite and calcite in the mid (123-115 Ma) and late (86-77 Ma) Cretaceous. Our results show that the brittle architecture of the study area is dominated by reactivation of ductile precursors and newly formed strike-slip faults, which is different from the dip-slip dominated brittle architecture of the southern section of the West Norway margin.

1. Introduction

Fractures and faults are common geological features in the upper crust. Onshore, fractures and faults represent zones of weakness with generally high erodibility, controlling the location of important landscape features such as valleys and fjords. Offshore, similar structures offset sedimentary packages, impacting the permeability and fluid and gas pathways, which have implications for hydrocarbon exploration and CO_2 storage projects. Understanding the formation and evolution of fault and fracture patterns in space and time is therefore an important task when we try to resolve the evolution of landscapes or to understand the pathways of fluids and gasses.

Western Norway has long been an important site for the study of rift processes and source to sink relationships along passive continental margins. The region is one key area where basement fault and fracture patterns both influence the onshore landscape and impact the distribution of sedimentary packages offshore (Redfield et al., 2005; Fossen et al., 2017, 2021; Scheiber and Viola, 2018). Deciphering the spatial and temporal evolution of complex fault and fracture patterns in metamorphic basement is challenging, and one needs to address the issues that follows: (a) the role of ductile structural precursors (e.g. Walsh et al., 2013; Skyttä & Torvela, 2018), (b) the role of reactivation of fault systems under changing stress fields (Redfield et al., 2005; Scheiber and Viola, 2018) and (c) complexities in interpreting K–Ar fault gouge data. The latter requires a good understanding of the thermal evolution of the study area and the complexity of fault zone architecture (Viola et al., 2016; Scheiber and Viola, 2018; Tartaglia et al., 2020).

In this study, we aim to unravel the spatial and temporal evolution of fault and fracture patterns in a so-far little-studied key area of Western Norway: the transitional area between the N–S trending North Sea margin in the south and the NE–SW trending Møre margin in the north (Fig. 1). We combine remote sensing lineament analysis with ductile foliation trace mapping to investigate the significance of ductile precursors for the subsequent brittle evolution. We then present an extensive field data set from brittle faults and fractures, highlighting the presence of both newly formed structures and structures reactivating

* Corresponding author.
E-mail address: ase.hestnes@uib.no (Å. Hestnes).

https://doi.org/10.1016/j.jsg.2022.104621
Received 17 December 2021; Received in revised form 8 May 2022; Accepted 10 May 2022
Available online 13 May 2022

older, ductile precursors. Observations of fault and fracture mineralizations help to constrain the relative timing of faulting activity, and K–Ar fault gouge data provide absolute age constraints on faulting. By applying different approaches of paleostress analysis to our dataset, we then suggest a spatial-temporal model for the brittle evolution of our study area. We show that the area is dominated by strike-slip kinematics and that prominent phases of rifting offshore are less prominent in the onshore realm.

2. Geological setting

The bedrock in the study area consists of the following elements (Fig. 1): 1) Proterozoic gneisses of the Western Gneiss Region (WGR) (e.g. Røhr et al., 2004, 2013; Corfu et al., 2014; Wiest et al., 2021), 2) Proterozoic and Paleozoic ortho- and paragneisses of the Caledonian nappes (e.g. Furnes et al. 1990; Corfu and Andersen 2002), and 3) Devonian sedimentary rocks (e.g. Osmundsen and Andersen 2001). The bedrock is highly influenced by the Caledonian orogeny with the subduction of parts of the WGR to ultra-high pressure depths in the Devonian (e.g. Hacker et al. 2003, 2010; Kylander-Clark et al. 2007), translation of the nappes during the collisional phase (e.g. Roberts and Sturt 1980; Hacker and Gans 2005; Corfu et al. 2014), subsequent extensional collapse (e.g. Fossen 1992, 2010; Krabbendam and Dewey, 1998) and the associated formation of the Devonian basins (e.g. Seranne and Seguret 1987; Osmundsen et al. 1998; Braathen et al. 2004).

2.1. Ductile precursor structures

The WGR and the overlying Caledonian nappes experienced extensive shearing, folding and doming during the collapse of the Caledonian orogen, starting at about 410 Ma and leading to the formation of the main ductile precursor structures in the study area (e.g. Fossen and Dunlap, 1998; Wiest et al., 2021). Several Devonian shear zones separate the orogenic root of the WGR from the overlying Caledonian nappes and the Devonian basins. The large-scale, corrugated detachment system of the Nordfjord-Sogn Detachment Zone (NSDZ; e.g. Labrousse et al., 2004; Young, 2018) connects with the Bergen Arc Shear Zone (BASZ) (e.g. Wennberg 1996) to the south (Fig. 1a). The Møre-Trøndelag Fault Complex (MTFC, Seranne, 1992), the Nordfjord Shear Zone (NSZ, Hacker et al., 2010) and the Lom Shear Zone (LSZ, Wiest et al. 2021) all

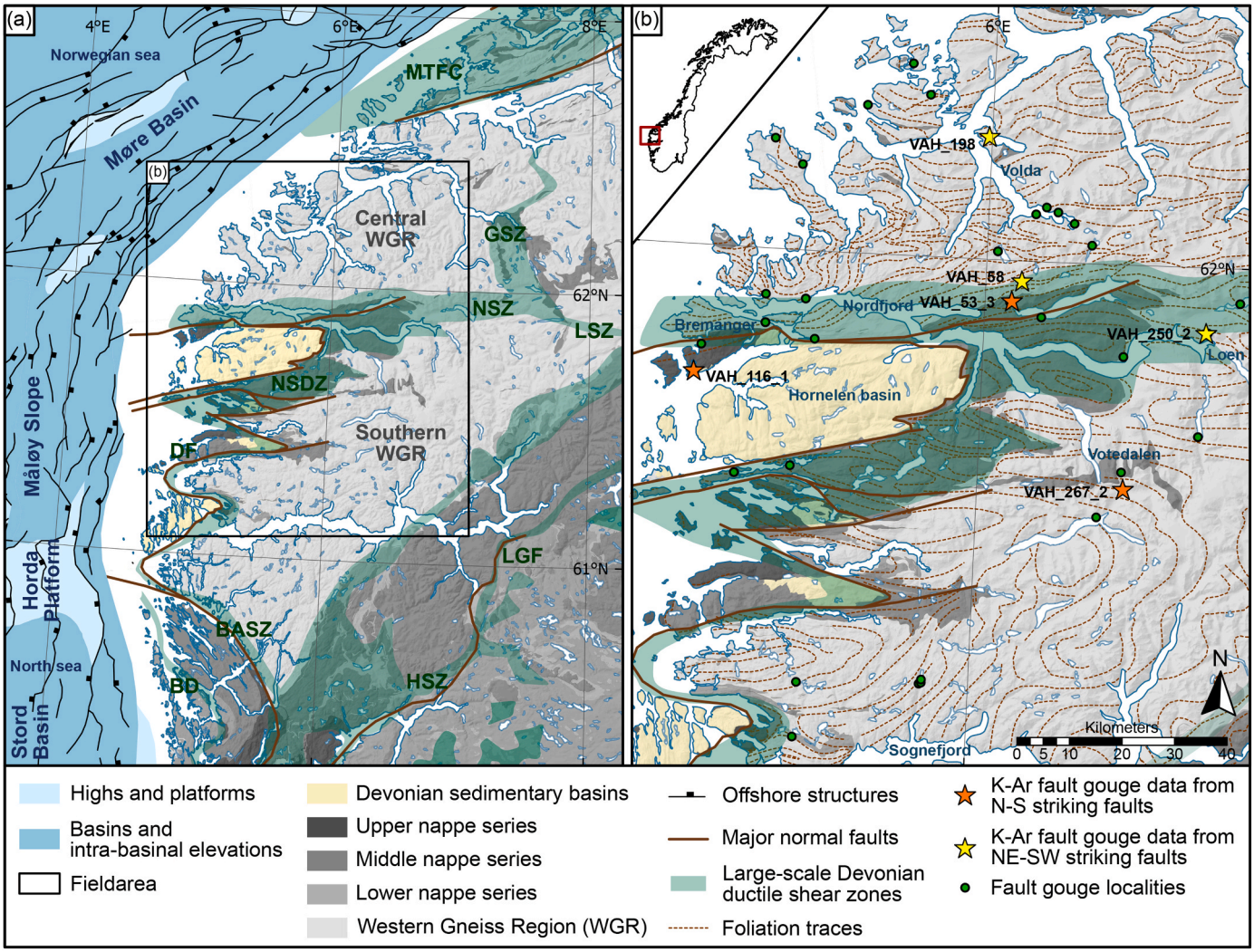

Fig. 1. (a) Simplified tectonic map of Western Norway showing offshore structures and onshore major shear zones (transparent green areas) and major faults (brown solid lines). BD= Bergen Detachment; BASZ=Bergen Arcs Shear Zone; DF = Dalsfjord Fault; GSZ = Geiranger Shear Zone; HSZ=Hardangerfjord Shear Zone; LGF = Lærdal-Gjende Fault; LSZ = Lom Shear Zone; MTFC = Møre-Trøndelag Fault Complex; NSDZ=Nordfjord-Sogn Detachment Zone; NSZ=Nordfjord Shear Zone. The black square indicates the study area. White offshore and coastal areas indicate basement highs. Map modified from Wiest et al. (2021). (b) Tectonic map of the study area. Red square on inset of Norway indicates the location of the study area. Stars indicate the location of dated K–Ar fault gouge samples (orange stars = N–S striking faults, yellow stars = NE-SW striking faults). Green dots indicate the location of sampled fault gouges that were not analysed in this study. Foliation traces modified from Wiest et al. (2021). (For interpretation of the references to colour in this figure legend, the reader is referred to the Web version of this article.)

show mostly ductile sinistral kinematics and acted as strike-slip transfer zones during transtensional collapse (Krabbendam and Dewey, 1998; Osmundsen and Andersen, 2001; Wiest et al., 2021). These structures are reflected in the regional foliation trends. Foliation trace mapping based on published foliation measurements shows E–W to NE–SW--striking foliations north of and along the Nordfjord, and E–W to NW–SE-striking foliations south of the Nordfjord, with several domes developed in the WGR (Figs. 2 and 3a; Wiest et al., 2021). The foliation is dominantly flat to gently dipping, but steeper dips occur as well (Supplementary 1).

2.2. Brittle faulting

From the Devonian onwards, the ductile structural pattern has been overprinted by repeated episodes of brittle faulting (Gabrielsen et al., 2002; Fossen et al., 2017, 2021; Ksienzyk et al., 2016; Scheiber and Viola, 2018), including the brittle reactivation of major ductile shear zones. North of the study area, the MTFC has shown repeated brittle activity in the Late Devonian, Permo-Triassic, Mid- and Late Jurassic, Cretaceous, and Cenozoic (Redfield et al., 2004, 2005; Osmundsen et al., 2006). Similar repeated activity has been documented from other regional faults: the Nordfjord-Sogn Detachment fault in the Permian and Jurassic-Cretaceous (Braathen et al., 2004), the Dalsfjord fault (DF) in Late Permian-Early Triassic, Jurassic, and Cretaceous times (Torsvik et al., 1992; Eide et al., 1994; Fossen et al., 2021), and the Lærdal-Gjende fault (LGF) in Permian, Late Jurassic-Early Cretaceous and the Paleocene (Andersen et al., 1999; Fossen et al., 2017; Tartaglia et al., 2020). Detailed analyses of minor fault zones and fracture patterns, mainly south of our study area, revealed early Carboniferous, Permian, Triassic-Jurassic, Cretaceous and Paleogene episodes of brittle faulting (Ksienzyk et al., 2014, 2016; Viola et al., 2016; Scheiber and Viola, 2018; Scheiber et al., 2019; Fossen et al., 2021).

2.3. Brittle evolution offshore

The onshore fault activity relates to two well-constrained phases of rifting in the North Sea (Steel and Ryseth, 1990; Roberts et al., 1995; Færseth, 1996): 1) rift phase 1 during the Permian and Early Triassic affecting a wide area and showing general E–W extension, and 2) the more localized rift phase 2 during the Late Jurassic and Early Cretaceous of which the extension direction is controversial. Several suggestions have been made for the latter, including E–W extension (Bartholomew et al., 1993; Reeve et al., 2015), NE–SW extension (Færseth, 1996; Færseth et al., 1997), or one or two phases of rotation throughout the rift phase (Doré et al., 1997; Davies et al., 2001). Similar phases of rifting have also been suggested for the Møre Margin in the Norwegian Sea (Talwani and Eldholm, 1972; Grunnaleite and Gabrielsen, 1995; Gómez et al., 2004; Theissen-Krah et al., 2017): 1) a first rift phase is constrained to early Permian-Early Triassic with a ENE-WSW extension direction, 2) a major NW–SE directed rift phase in Late Jurassic and Early Cretaceous, suggested to have ended by mid-Cretaceous, and 3) a last stretching event in Late Cretaceous and Palaeocene leading to the final break-up between Greenland and Eurasia in the Eocene. In this study, we aim at deciphering the structural evolution of the onshore transition zone between the North Sea and the Norwegian Sea rift systems.

3. Methods

3.1. Remote sensing

We conducted foliation trace analysis and lineament mapping in ArcGIS to acquire an overview of the structural architecture of the region. We used foliation traces drawn by Wiest et al. (2021), which were manually interpolated between field measurements of foliations stored in the 1:50 000 and 1:250 000 bedrock map database of the Geological Survey of Norway (NGU). Manual extraction of lineaments is a qualitative method where the results depend on the operator, what map sources are used, and the scale used for mapping (Scheiber et al., 2015). Manual extraction of lineaments was conducted by the first author on digital elevation models (DEMs) and on vertical derivatives of the topography which is a map source not sensitive to illumination direction and was made in Seequent Oasis Montaj (Supplementary 2). Orthophotos were used to study specific lineaments in more detail and, in some cases, hillshaded DEMs were used for further analysis.

A conservative approach was applied where only distinct linear topographic bedrock features that clearly represent the expression of brittle bedrock structures were included in the lineament map (see Supplementary 2). Lineament mapping was performed at three different scales (1:300 000, 1:200 000 and 1:100 000) and is presented as a synthesis map with lineaments from all scales (Fig. 2).

3.2. Structural field work

Our foliation trace and lineament analysis served as a base for choosing areas for fieldwork. In the field, we systematically collected fault and fracture data, including orientation, slip line orientation, fault rock type, fracture surface mineralization, sense of slip, geometric relation to the local foliation, and if present, signs of reactivation. For the sense of slip, we attributed each fault-slip measurement with a value based on confidence and preservation (C – certain, P – probable, S – supposed, X – unknown). We also collected fault gouge samples for K–Ar geochronology.

3.3. K–Ar fault gouge dating

The K–Ar fault gouge analyses including separation into grain size fractions, XRD characterization and K–Ar dating were carried out at the Geological Survey of Norway and a detailed method description is provided in the supplementary material (Supplementary 3). The samples were separated into five grain size fractions before dating: 6–10 μm, 2–6 μm, 0.4–2 μm, 0.1–0.4 μm and <0.1 μm. The mineralogical composition of each fraction was determined by X-ray diffraction (XRD). The XRD patterns were also inspected in terms of possible illite polytypes that may represent different generations of illite (Grathoff and Moore, 1996).

To study the mineralogical and crystallographic properties of the fault gouge samples, we used scanning electron microscopy (SEM) at the Elmilab, University of Bergen. The gouge samples were first encapsulated in epoxy and surfaces were polished. Backscatter electron imaging (BSE) was done using a Zeiss Supra 55 VP. Element mapping and energy dispersive X-ray analysis (EDX) was done by using a Thermo Fisher X-ray detector and the Pathfinder software. Only the fractions of 2–6 μm and 6–10 μm were studied under the SEM. The other fractions were too fine grained and did not reveal any useful information.

3.4. Paleostress analysis

Observations of a brittle fault's plane and slip line orientation together with kinematic information can be used to deduce a local stress tensor under which the fault has formed (Angelier, 1979; Lacombe, 2012; Simón, 2019). When performing paleostress analysis, the measured kinematic data are inverted into a single reduced stress tensor. The stress tensor provides information about the orientation of the principal stress axes ($\sigma_1 \geq \sigma_2 \geq \sigma_3$) and the stress ratio R. R indicates the relative magnitude of the principal stresses and is defined as $(\sigma_2 - \sigma_3)/(\sigma_1 - \sigma_3)$ (Angelier, 1984).

To perform paleostress analysis, we used the program WinTensor by Delvaux and Sperner (2003). The dataset was divided into local stations based on location size and number of included fault and fracture measurements. In Win Tensor, we did the following procedure: First, we applied the Right Dihedron method, which finds the best fit stress tensor for a given number of field measurements and which removes outliers.

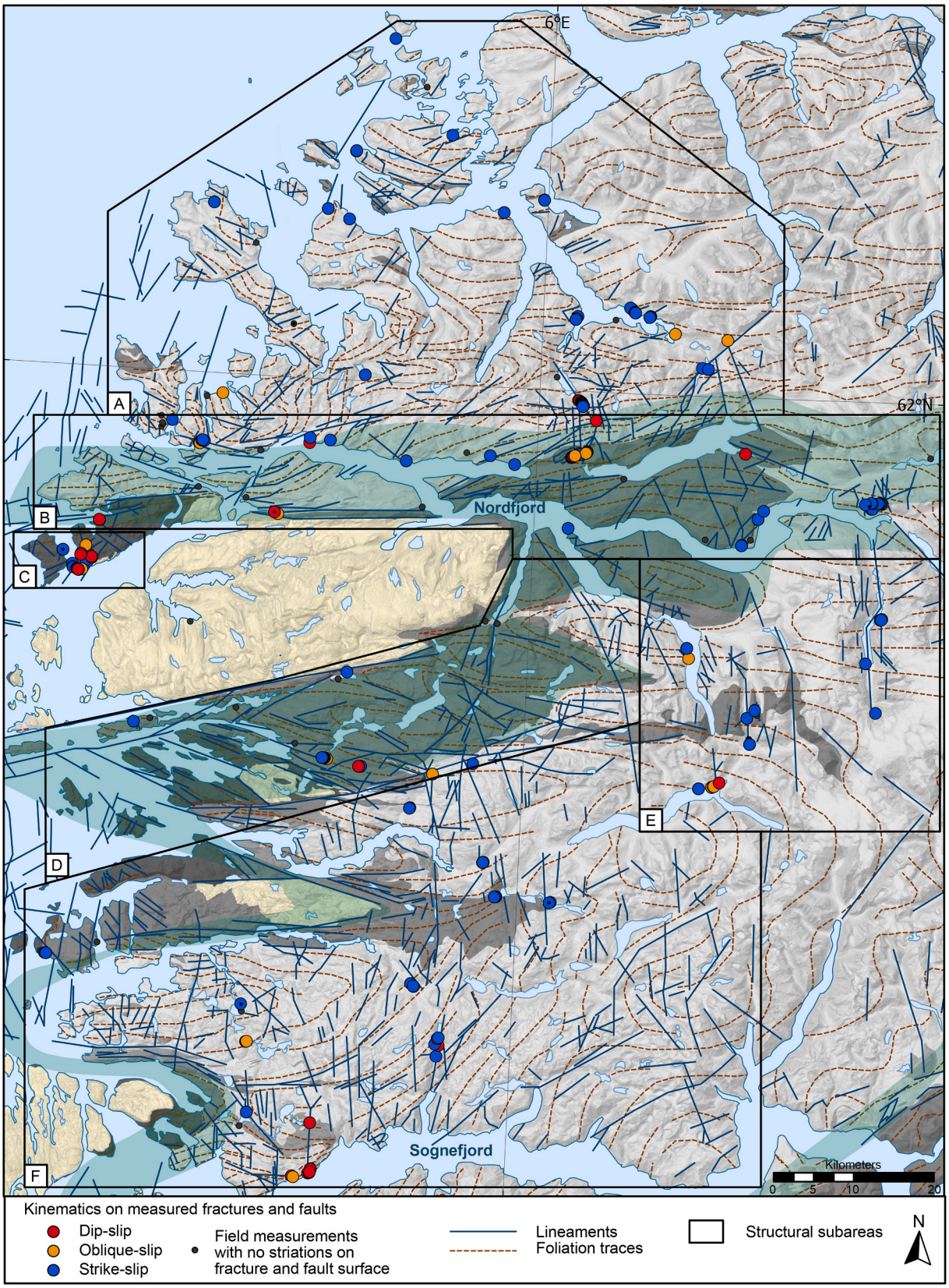

Fig. 2. Map with foliation traces (stippled brown lines, modified from Wiest et al. 2021) and manually extracted lineaments (blue lines). Lineaments represent a compilation extracted from DEMs and the vertical derivatives of the topography at three different scales (1:300 000, 1:200 000 and 1:100 000). Based on overall structural characteristics, the study area is divided into six subareas indicated by black boxes labelled A-F. Coloured circles indicate orientation of the observed lineation along brittle faults (red = dip-slip; orange = oblique slip; blue = strike-slip), whereas black dots correspond to localities where no kinematic indicators were observed. A total of 620 field localities are included. (For interpretation of the references to colour in this figure legend, the reader is referred to the Web version of this article.)

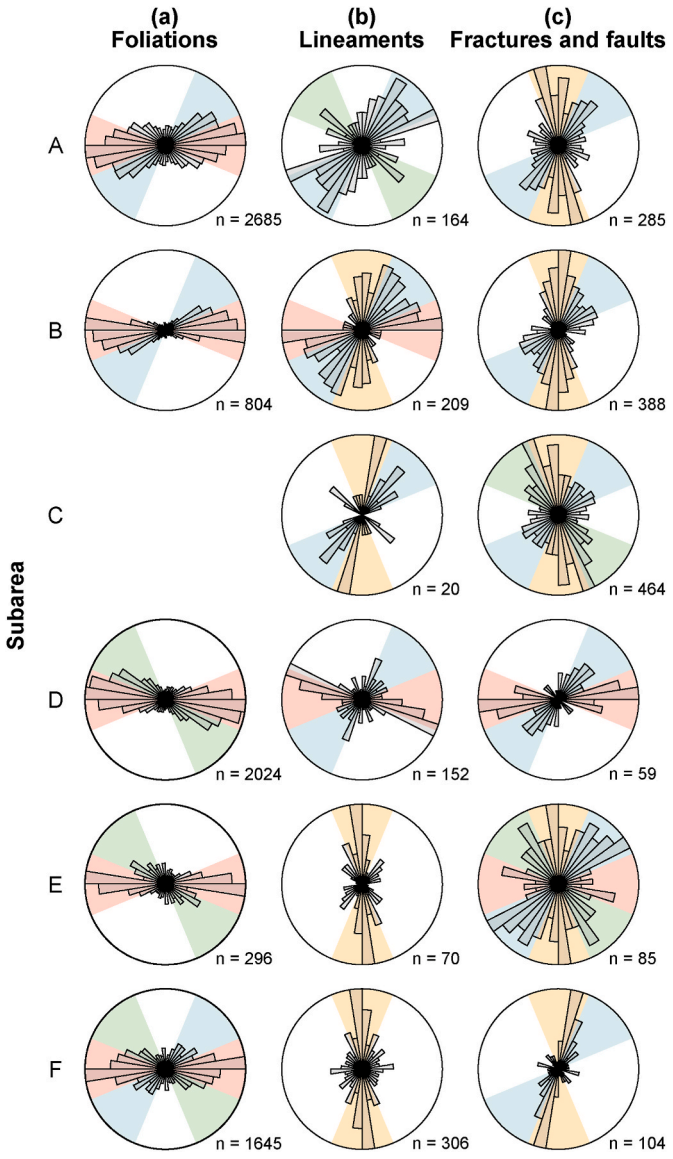

Fig. 3. Strike orientation of structural data from subareas A-F (Fig. 2) shown as number weighted rose plots (bin size 40). (a) Foliation measurements from the structural database of NGU. (b) Lineament trends. (c) Fractures and faults measured in the field, also those not containing observed surface mineralizations. Background colours shows the main groups of strike orientation for each plot (yellow = N–S; blue = NE-SW; pink = E-W; green = NW-SE). Subarea C represents the Bremanger Granitoid Complex which lacks ductile foliation. (For interpretation of the references to colour in this figure legend, the reader is referred to the Web version of this article.)

The selected stress tensor was further analysed with the Rotational Optimization method, where the stress tensor is iteratively adjusted to the data set. During this step, fault planes containing slip lineations but lacking information about sense of movement were also included. For each subset, measurements exceeding an alpha misfit angle of 17° were rejected as suggested by Simón (2019). Alpha is the angle between the measured slip line and the theoretical slip direction according to the resolved shear stress on the plane. To evaluate the resulting stress field, we used the modified stress index regime R' (Delvaux and Sperner, 2003). R′ is a numerical parameter ranging from 0 to 3: extensional stress regime (σ_1 vertical) when R' = R; strike-slip stress regime (σ_2 vertical) when R' = 2 – R; and compressional stress regime (σ_3 vertical) when R' = 2 + R (Delvaux and Sperner, 2003). The following five categories of stress tensors are used (after Mattila and Viola (2014)): pure extension, R' = 0–0.75, transtension, R' = 0.75–1.25, pure strike-slip, R' = 1.25–1.75, transpression, R' = 1.75–2.25, and pure compression, R' = 2.25–3.

Following the first order paleostress analysis at the local stations, we perform significance tests for the individual local stress tensors according to Orife and Lisle (2006). We arrange the test results according to amount of included fracture and fault measurements and the average alpha value. Further, we categorize the individual measurements of each station by fault surface mineralization and redo the paleostress analysis. The resulting local stress tensors are again tested according to Orife and Lisle (2006), a procedure suggested by Simón (2019).

4. Results

Based on the large-scale ductile architecture of the study area, we divide the study area into six subareas (Fig. 2): subarea A encompasses the area north of the NSDZ and NSZ; subarea B comprises the area along Nordfjord including the NSZ and parts of the NSDZ; subarea C represents the Bremanger Granitoid Complex dated to 440 ± 5 Ma (Hansen et al., 2002), which does not contain a ductile precursor foliation due to its high structural position within the Caledonian nappe stack; subarea D comprises the NSDZ south and east of the Hornelen Devonian basin; subarea E encompasses the most inland parts of the study area dominated by N–S trending valley systems; and subarea F includes the southernmost part of the field area east of the NSDZ and north of the Sognefjord.

4.1. Lineament mapping

Fig. 2 shows the lineaments identified within the different subareas. Three main lineament orientation trends are visible (Fig. 3b): 1) N–S (yellow in Fig. 3), 2) NE–SW (blue in Fig. 3) and 3) E–W (red in Fig. 3). In subarea A, the NE–SW trend dominates, whereas in subareas B and D, the E–W trend dominates, following mainly the trend of the ductile foliation. In subareas C, E and F, the N–S trend dominates, clearly cutting the trend of the main foliation (Fig. 3a and b).

4.2. Field observations

We collected structural data from brittle faults and fractures at 620 field localities, representing 1385 individual fault and fracture surfaces with fault mineralizations and 452 slip lines on fault planes (Fig. 2, Supplementary 4). In general, the three main orientation trends identified from lineament mapping are also present in the field measurements within each subarea, except for the E–W trend in subarea B, which is missing in the field data (Fig. 3b and c). The E–W lineament trend in subarea B is therefore more likely an effect of the pervasive E–W ductile foliation trend (Fig. 3a). In addition, the field measurements show that N–S striking faults and fractures are more pronounced throughout the study area than what the lineament mapping shows, except for subarea D, where this trend is missing in the field data as well (Fig. 3b and c). The NW–SE striking fractures and faults are minor in all subareas (green in Fig. 3).

At each location, we studied the relationship between the orientation of brittle faults and fractures and the local foliation. In subareas A, B and F, the NE–SW fractures strike generally parallel to subparallel to the local foliation, whereas in subareas D and E, the E–W brittle structures strike parallel to subparallel to the foliation. In general, the dip of the foliation is moderate to shallow, which is different from the steep dip of the fractures and faults (Supplementary 1). The N–S striking faults and fractures cut the local foliation throughout the study area.

The dip of the measured faults and fractures is generally steep (Fig. 4 and Supplementary 1). The slip line trends vary throughout the study area, depending on the strike of the corresponding faults, with a generally shallow plunge (Fig. 4). Slip line orientations show predominantly strike-slip kinematic indicators, with 248 strike-slip dominated

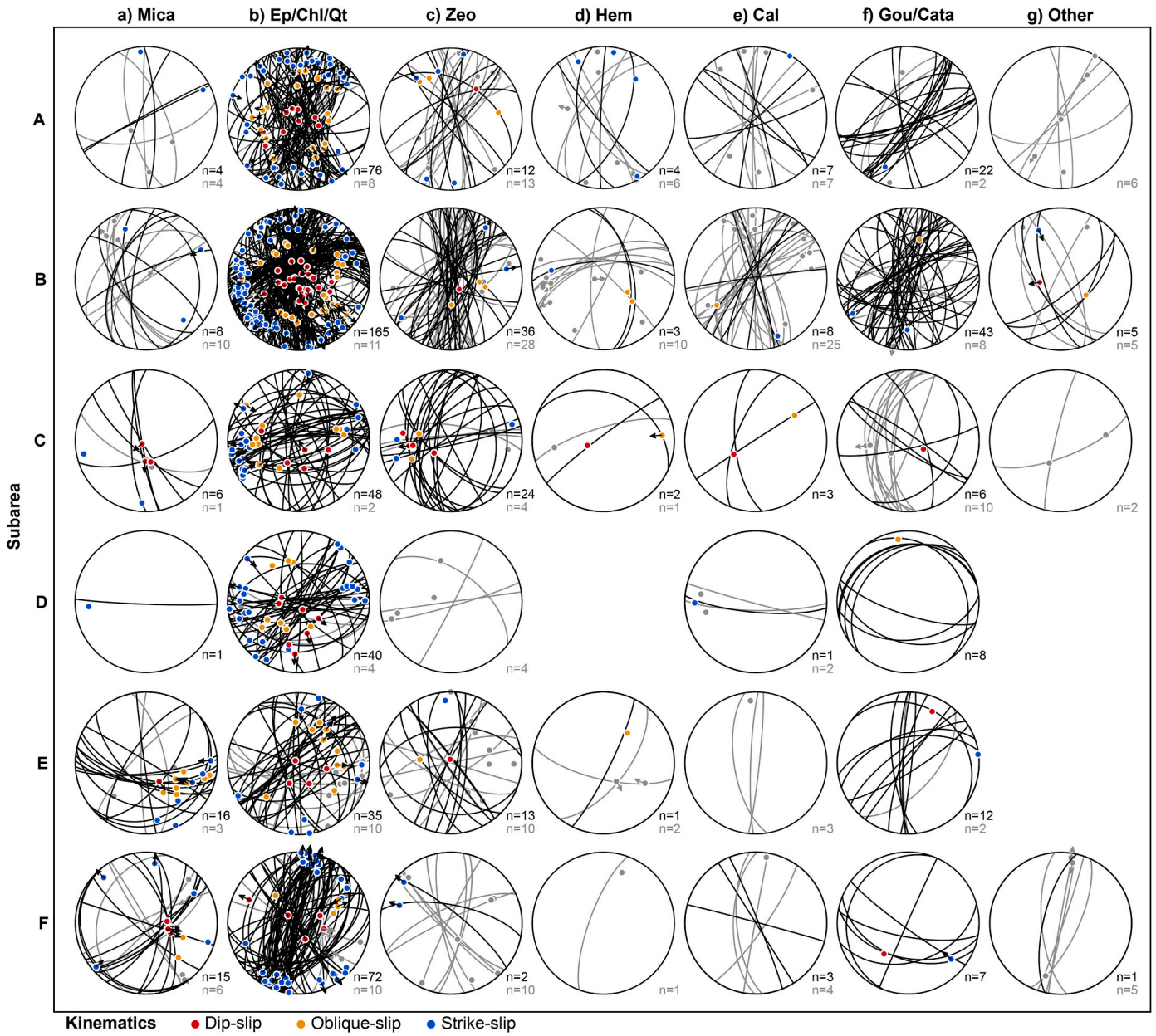

Fig. 4. Stereoplots of all measured fracture and fault surfaces with mineral coatings and/or cataclasite/gouge from the study area. A-F correspond to subareas from Fig. 2. The measurements are grouped according to their mineral coating and/or whether they are associated with cataclasite/gouge. Ep = epidote; Chl = chlorite; Qt = quartz; Zeo = zeolite; Hem = hematite; Cal = calcite; Gou = gouge; Cata = cataclasite. Black and coloured (red = dip-slip dominated kinematic indicators (dip 90-60°); orange = oblique-slip dominated kinematic indicators (dip 60-30°); blue = strike-slip dominated kinematic indicators (dip 30-0°)) measurements indicate surfaces dominated by the main mineral within each category, whereas grey measurements represent surfaces where the mineral of the category is a minor constituent; these grey surfaces appear as well within the plot of the dominating mineralization. (For interpretation of the references to colour in this figure legend, the reader is referred to the Web version of this article.)

faults, 125 oblique-slip faults and 79 dip-slip dominated faults observed (Fig. 2).

Based on observed fault and fracture mineralizations, we assigned our field measurements to seven different groups, sorted according to inferred high-to low-temperature mineralizations (Figs. 4 and 5): 1) Discrete fracture surfaces characterized by aligned muscovite/biotite and/or stretched quartz, feldspar and hornblende (stretched host rock, SHR) were mostly observed in subareas B, E and F (Figs. 4a and 5a). The stretching of these minerals must have happened under relatively high-temperature and thus semi-ductile conditions. These surfaces are, in places, covered by epidote, chlorite and/or quartz mineralizations (Fig. 5b). SHR surfaces have variable dip angles and they have been found both cutting and being parallel to the foliation with variable strike orientation (Fig. 4a). The observed kinematic indicators are mainly dextral or sinistral strike-slip to oblique-slip. 2) Surfaces with epidote, chlorite and/or quartz are the most common mineralizations in all subareas (Figs. 4b and 5c). These surfaces do not show clear orientation trends. Steeply dipping surfaces showing slip lines with shallow plunge and strike-slip movements seem to be more abundant. Some of these surfaces contain two generations of slip lines (Fig. 5d). 3) Surfaces with zeolite mineralizations occur throughout the study area (Fig. 4c). The zeolite mineralizations vary in colour from white to pink to orange and occur as euhedral radial crystals or as striated fibres (Fig. 5e–g). Zeolite often occurs on top of epidote and chlorite mineralizations and is the apparent younger mineral (Fig. 5e). The zeolite surfaces are commonly steeply dipping and generally strike N–S or NE–SW to E–W, and when

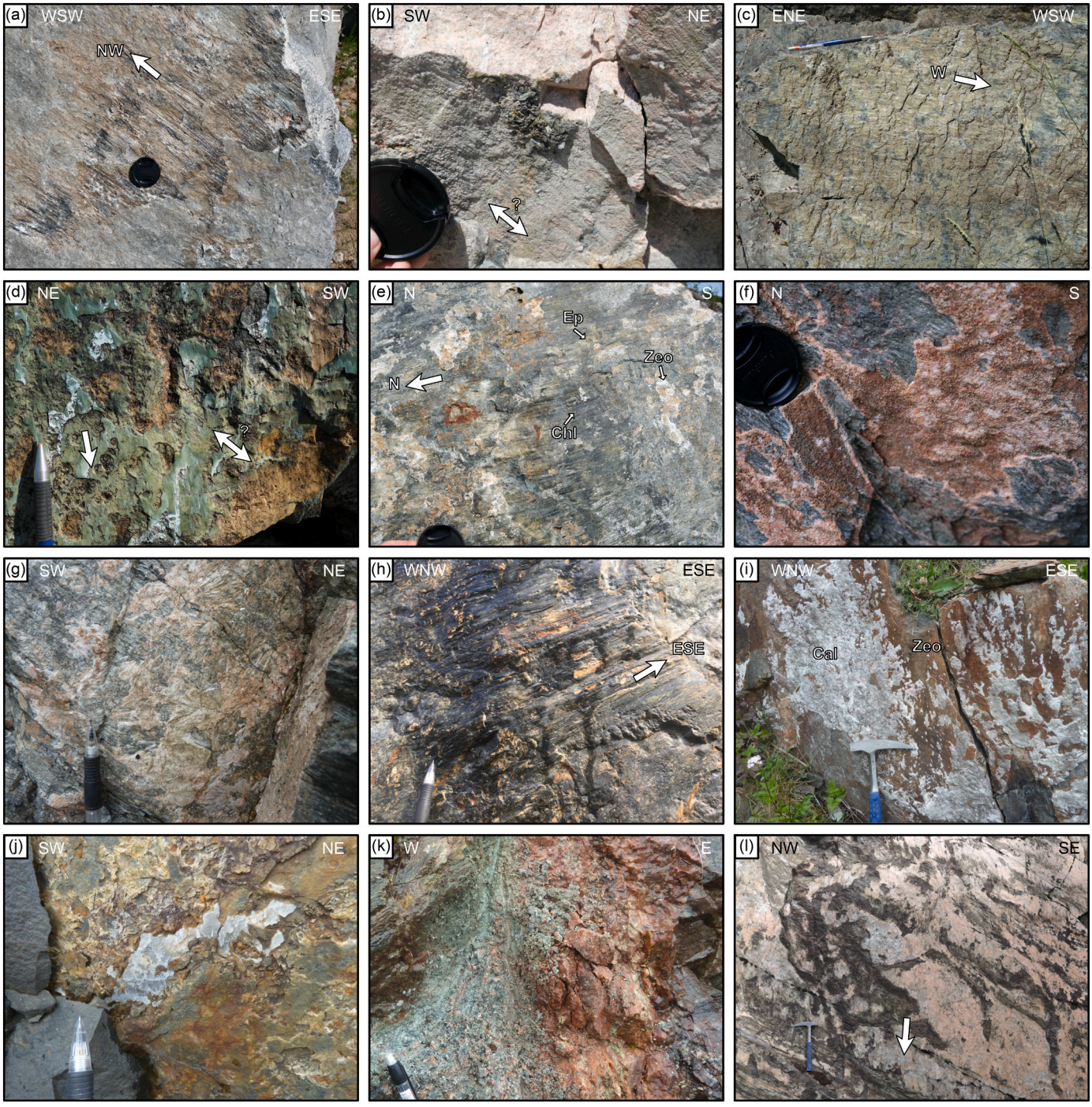

Fig. 5. (a) Semi-ductile strained fault surface with stretched amphibole and muscovite mineralization (all coordinates of localities here and in the following UTM 32N: 364324/6828098). Arrow indicates sinistral shear. (b) Semi-ductile strained fault surface with stretched feldspar and quartz rods and with chlorite, epidote, and quartz crystals on top (364340/6828103). Arrow indicates shear, direction unknown. (c) Epidote and chlorite mineralization with slickensides (347502/6869635). Arrow indicates dextral shear. (d) Fault in serpentinite showing two generations of slickensides on epidote- and chlorite-coated surface (321049/6879673). Shear sense of older slip line is unknown. Arrow indicates normal shear on younger slickenside. (e) Striated fracture surface with chlorite and minor epidote (384313/6863612). Arrow indicates sinistral shear. Patches of white zeolite on top, also showing sinistral shear. (f) Pink-orange zeolite crystals on the fracture surface, no slip line developed (368751/6836728). (g) Pale pink radial zeolite crystals on fracture surface (368751/6836728). (h) Striated hematite- and chlorite-coated surface (280996/6807453). Arrow indicates dextral shear. (i) Fracture surface coated with zeolite (orange to pink) and calcite (white) (324866/6921786). Zeolite is found both below the calcite and in small patches above the calcite. (j) Fracture in the Kalvåg Melange on Bremangerlandet with white calcite (283257/6857875). (k) Zoned cataclasite (385183/6863538). Dark green – chlorite; light green – epidote; white – quartz and patches of calcite; pink; altered host rock and zeolite. (l) Fracture in peridotite coated with pale orange talc (316692/6871528). Arrow indicates normal shear. (For interpretation of the references to colour in this figure legend, the reader is referred to the Web version of this article.)

found alone, they rarely show any slip lines (Fig. 4c). 4) Surfaces with hematite are more common in the northern field area and are commonly found together with dark green chlorite (Figs. 4d and 5h). These surfaces have similar orientations and sense of shear as the surfaces with epidote, chlorite and/or quartz (grey, Fig. 4d). 5) Surfaces with calcite (Fig. 5i–j) are most common in subarea B (Fig. 4e). The calcite appears as thin mineral coatings or as bigger crystals, and both alone on surfaces or together with any of the above-mentioned mineralizations. If occurring together with other mineralizations, calcite is normally found on top and seems to be the younger mineral (Fig. 5i). We rarely observed slip lines on calcite, and no kinematic indicators were observed (Fig. 4e). 6) Faults containing cataclasite and/or uncohesive fault rock such as breccia and gouge occur throughout the study area, with most observations in subarea B (Figs. 4f, 5k and 6). These faults show variable orientations with shallow to steep dips. Slip lines and kinematic indicators were rarely observed on the fault surfaces in direct contact with the gouge. If observed, it was commonly seen on other surface minerals and is plotted in the corresponding mineral stereoplot in Fig. 4 and only shown in grey for Fig. 4f. The observed cataclasites represent 5–80 cm thick zones of crushed host rock containing minerals like chlorite, epidote, K-feldspar, and zeolite (Fig. 5k). 7) A smaller group of faults contains other minerals like talc, K-feldspar or pyrite (Figs. 4 and 5l).

4.3. K–Ar gouge dating

In total, 56 gouges from 43 different faults were sampled (Fig. 1b). We collected gouges from all the three main fracture orientation trends observed (Figs. 3c and 4f). Six samples from the two most dominant gouge-bearing fault sets were selected for K–Ar gouge dating (i.e., N–S and NE–SW trending, representing the trend of the North Sea and Møre margins, respectively). For both the N–S and NE–SW trending fault sets, we chose to analyse three samples representing the coastal, central and inland region of the study area, respectively (Fig. 1b). Detailed results from XRD analyses are shown in Supplementary 5.

4.3.1. N–S striking faults

4.3.1.1. VAH_116_1. Sample VAH_116_1 is from a W-dipping fault in the unfoliated Bremanger granodiorite that is exposed within a quarry (Figs. 1b and 6a). The main fault plane dips moderately towards the W (263/39, dip azimuth/dip) and contains slip lines oriented 263-45 (plunge direction-plunge) associated with normal (W-down) dip-slip kinematic indicators. Slickensides were observed on striated white zeolite on the fault plane. The sharp fault scarp can be followed for about 150 m, and the width of the exposed fault core is ca. 1–1.5 m (Fig. 6a). At the sample locality, the fault core consists of fault breccia with variable clast sizes, layers of gouge as well as layers of coarse-grained orange zeolite crystals. We sampled a ca. 3–6 cm thick gouge layer close to the hanging wall (Fig. 6a). The three larger grain size fractions contain smectite, quartz, K-feldspar, chlorite, illite/muscovite and plagioclase (Fig. 7a). BSE imaging of the coarsest fraction shows smectite replacing K-feldspar crystals (Fig. 7a). The two finest grain size fractions of the sampled gouge consist of smectite with possible traces of illite/muscovite. Palygorskite may also be present as inferred from its characteristic peak at 10.4 Å (Supplementary 6). The K–Ar dates show a slightly convex-upward age spectrum ranging from 155 ± 2 Ma for the coarsest fraction (6–10 μm) to 115 ± 2 Ma for the finest fraction (<0.1 μm) (Table 1, Fig. 8a).

4.3.1.2. VAH_53_3. Sample VAH_53_3 is from a fault zone located along Rv651 north of Nordfjord (Figs. 1b and 6b). The host rock is a banded gneiss with a foliation oriented 128/56. The fault itself measures 075/85 with slip lines oriented 159-15. The fault shows strike-slip movement through slip lines on calcite but kinematic indicators were not observed. The fault consists of one 10–40 cm wide fault strand containing gouge and clasts of host rock and calcite. All grain size fractions are poorly crystalline as shown by broad diffractions peaks with low intensities. The two coarser fractions of the sampled gouge contain mainly smectite with subordinate K-feldspar, chlorite and minor quartz, whereas the three finest grain size fractions are entirely dominated by smectite (Table 1; Fig. 7b). The finest fraction is monomineralic. BSE imaging of the coarsest fraction shows K-feldspar with smectite replacement textures (Fig. 7b). The K–Ar dates show an inclined age spectrum with dates ranging from 124 ± 2 Ma for the coarsest fraction (6–10 μm) to 86 ± 2 Ma for the finest fraction (<0.1 μm) (Table 1, Fig. 8a). The three coarsest fractions overlap within their uncertainties with a mean age of 123 ± 2 Ma.

4.3.1.3. VAH_267_2. Sample VAH_267_2 is from a fault zone located along E39 at the southern end of Votedalen (Figs. 1b and 6c). The monzonitic host rock has a foliation oriented 125/30. The entire outcrop is cross-cut by subvertical fractures coated with pink zeolite crystals and, in some places, calcite minerals in the centre (Fig. 6c, insert). There are two zones of fault breccia, where one also contains gouge. The orientation of the gouge-bearing zone is 261/65 with a slip line of 355-13. The fault shows strike-slip movement on striated pink zeolite but kinematic indicators were not observed. The brecciated zone also contains epidote. Only four grain-size fractions could be extracted from the gouge sample (Table 1, Fig. 7c). The three coarser fractions of the sampled gouge contain smectite, illite/muscovite, plagioclase, zeolite, pyroxene, quartz, chlorite, and minor rutile, whereas the finest grain size fraction is monomineralic and consists entirely of smectite (Table 1, Fig. 7c). From XRD, the two coarsest fractions contain the 2M1 illite polytype (Supplementary 6). The K–Ar dates show an inclined age spectrum ranging from 240 ± 3 Ma for the coarsest fraction (6–10 μm) to 158 ± 4 Ma for the finest fraction (0.1–0.4 μm) (Table 1, Fig. 8a).

4.3.2. NE–SW striking faults

4.3.2.1. VAH_198. Sample VAH_198 is from a fault zone located along road 653 close to Volda (Figs. 1b and 6d). The host rock is a dioritic gneiss with a foliation oriented 071/47. The fault is located close to a lens of amphibolitic gneiss. The fault zone is approximately 2 m wide and consists of five fault branches, where two of these contain gouge and are separated by fractured host rock (Fig. 6d). The sampled fault has an orientation of 122/80 and a slip line of 204-25. The fault shows strike-slip movement on striated K-feldspar, but no sense of shear was observed. The coarser fractions of the sampled gouge contain biotite, smectite, K-feldspar, chlorite, plagioclase, zeolite and traces of amphibole, whereas the finest grain size fraction consists of biotite, chlorite and smectite (Fig. 7d). Biotite was identified with XRD according to its 5 Å/10 Å peak proportion (Supplementary 6). The presence of biotite is also supported by chemical data from ICP-OES analyses which show high concentrations of both Fe and Mg in contrast to Al. The smectite content decreases with decreasing grain size fraction, whereas biotite content increases (Fig. 7d). BSE imaging from the coarsest fraction shows fractured K-feldspar decomposing along its rims (Table 1, Fig. 7d). The K–Ar dates show a slight convex-upward age spectrum ranging from 194 ± 2 Ma for the coarsest fraction (6–10 μm) to 180 ± 2 Ma for the finest fraction (<0.1 μm) (Table 1, Fig. 8b).

4.3.2.2. VAH_58. Sample VAH_58 is from a fault zone located along road Rv651 north of Nordfjord close to a major NE–SW trending lineament crossing the valley (Figs. 1b and 2). The host rock is a banded gneiss with a foliation of 134/61. The fault zone is about 1 m wide and exhibits two slip planes containing incohesive fault rock and having sharp boundaries to the host rock (Fig. 6e). The orientation of the sampled fault is 122/55 with a slip line of 122-55. The fault shows dip-slip movement on striated K-feldspar, but kinematic indicators were not observed. The fault zone shows K-feldspar mineralization on the fault

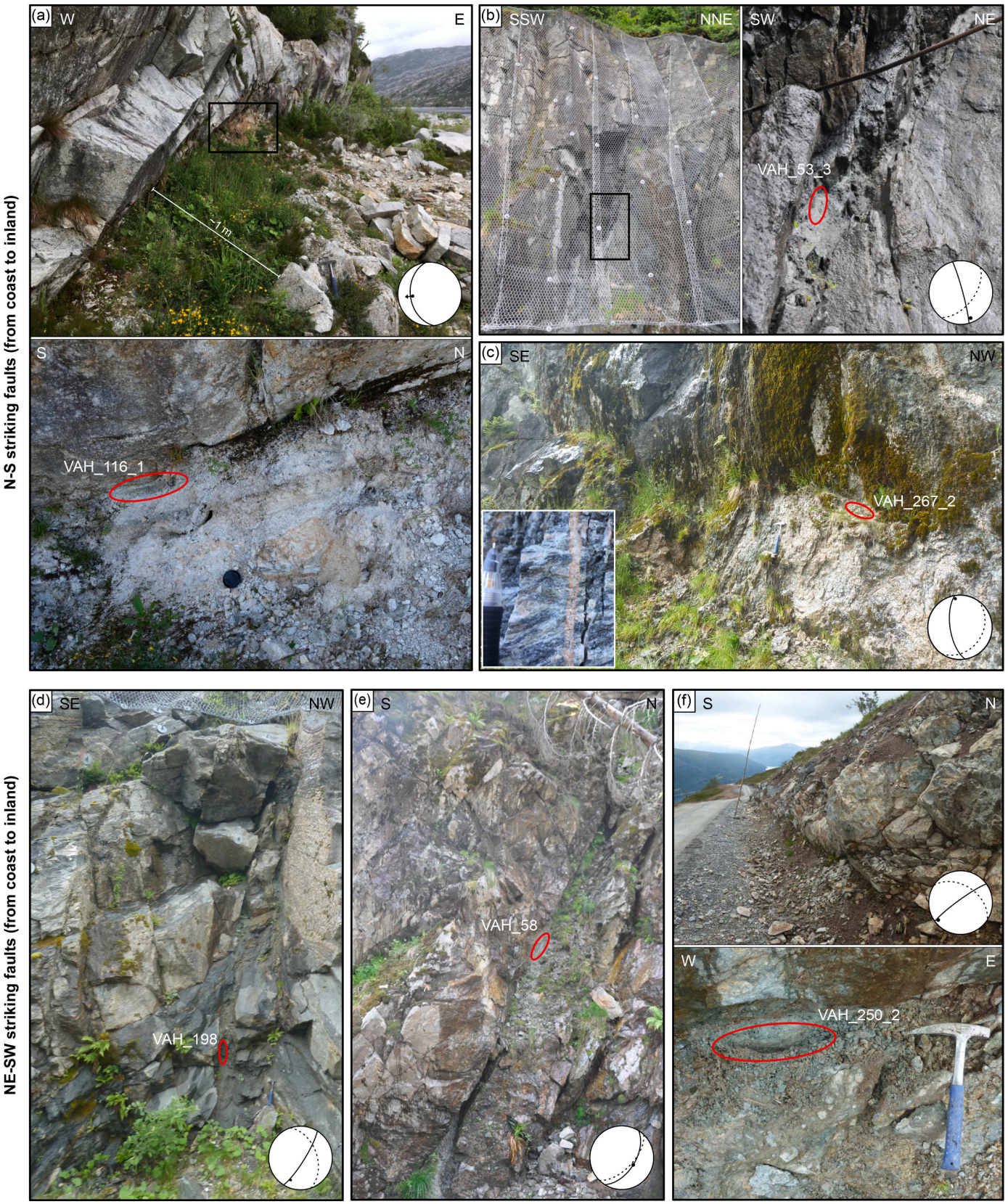

Fig. 6. Field photographs of dated (a–c) N–S striking faults and (d–f) NE-SW striking faults. The red circle marks the sample locality for K–Ar fault gouge dating. Stereoplots show structural measurements for each fault (stippled black great circle = foliation at sample location; black great circle = fault plane; black dot = slip line measured on host rock on the boundary to the sampled gouges; black arrow = observed kinematic indicators). (For interpretation of the references to colour in this figure legend, the reader is referred to the Web version of this article.)

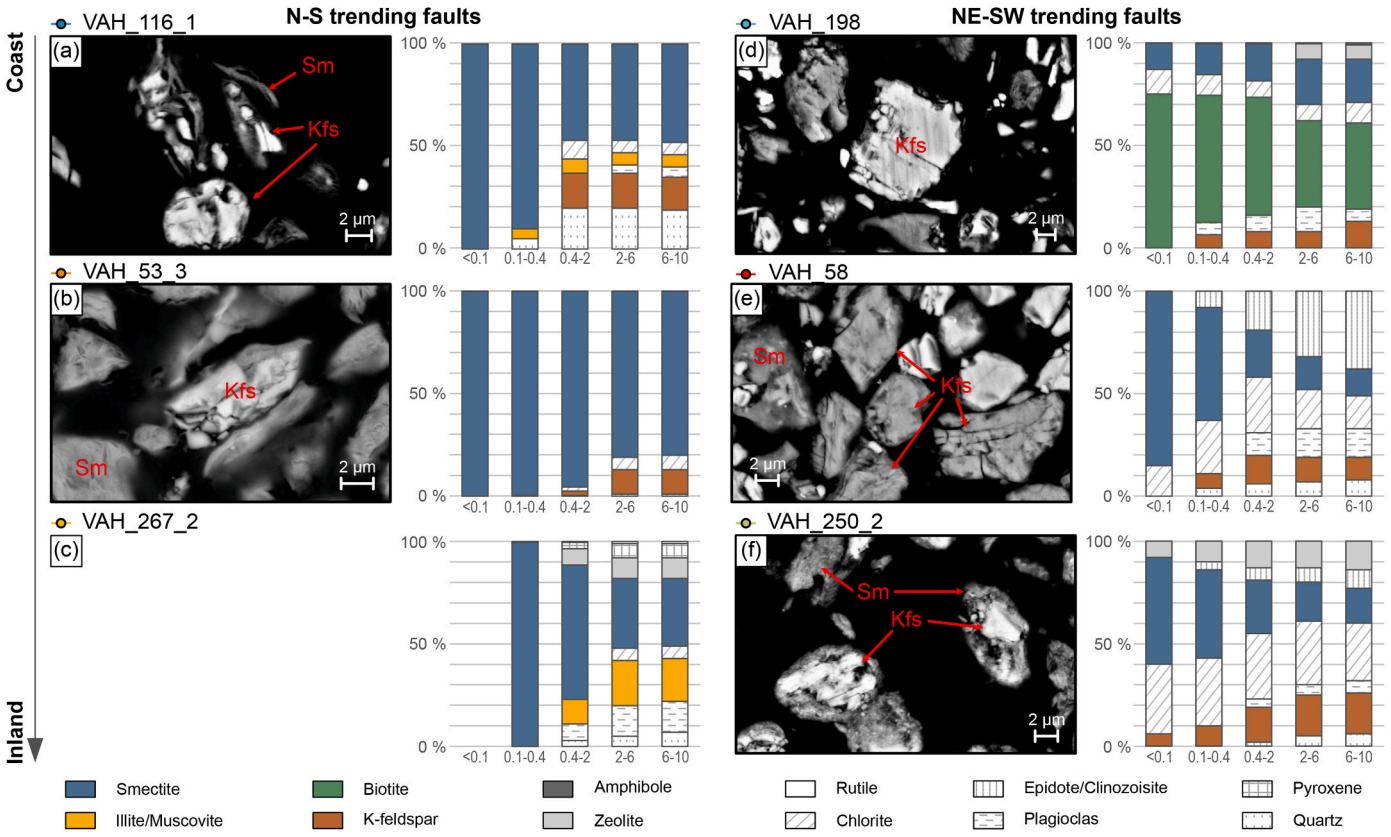

Fig. 7. XRD data from the dated gouge samples (cf. Supplementary 5 and 6) and corresponding BSE photographs of the 6–10 µm fractions. Minerals are indicated in red (Kfs = K-feldspar; Sm = smectite). (For interpretation of the references to colour in this figure legend, the reader is referred to the Web version of this article.)

surface. The coarser fractions of the sampled gouge contain epidote/clinozoisite, chlorite, smectite, plagioclase, K-feldspar and quartz, whereas the finest fraction consists mainly of smectite, with minor chlorite (Fig. 6e). BSE imagining from the coarsest fraction shows fractured and cracked K-feldspars (Fig. 6e). The K–Ar dates show an inclined age spectrum ranging from 191 ± 2 Ma for the coarsest fraction (6–10 µm) to 77 ± 1 Ma for the finest fraction (<0.1 µm) (Table 1, Fig. 8b).

4.3.2.3. VAH_250_2. Sample VAH_250_2 is from a fault zone exposed along the construction road to the top of the Loen skylift at the innermost Nordfjord (Fig. 1b). The host rock is a monzonitic augen gneiss with a foliation oriented 033/46. A 5–6 m long fault scarp is exposed along the road (Fig. 6f). The fault measures 336/60 and the slip line is 261-19. The fault shows strike-slip movement on a fault surface containing striated chlorite, quartz and white to orange zeolite, but kinematic indicators were not observed. The fault plane bends off from an about 2 m wide zone of cataclastic rock containing clasts of the host rock, epidote, chlorite, zeolite, K-feldspar, and calcite in a matrix of epidote, chlorite, zeolite, K-feldspar and quartz (Fig. 5k). The sampled gouge layer is 10–15 cm thick and is partly covered with superficial deposits (Fig. 6f). The coarser fractions of the sampled gouge contain chlorite, K-feldspar, smectite, zeolite, epidote/clinozoisite, plagioclase and quartz, whereas the finest grain size fraction consists of smectite, chlorite, zeolite and K-feldspar (Fig. 7f). BSE imaging of the coarsest fraction shows K-feldspar being replaced by smectite (Fig. 7f). The K–Ar dates show an inclined age spectrum ranging from 241 ± 3 Ma for the coarsest fraction (6–10 µm) to 129 ± 3 Ma for the finest fraction (<0.1 µm) (Table 1, Fig. 8b).

5. Interpretation

5.1. Interpretation of K–Ar fault gouge age spectra

In recent studies, the "Age Attractor Model" (Torgersen et al. 2015a; Viola et al. 2016) has been used to explain how an inclined age spectrum (K–Ar age vs. grain size fraction) defines a mixing curve between two end-members; the coarsest grain size fraction representing inherited host rock or early grown K-bearing minerals, and the finest grain size fraction representing K-bearing minerals formed under the last detectable faulting/fluid alteration event. The amount of authigenic K-bearing mineral phases increases with decreasing grain size and the finest fraction (here <0.1 µm) is generally interpreted to represent the last event of faulting (Torgersen et al., 2015a; Viola et al., 2016; Tartaglia et al., 2020). This model serves as a useful first-order interpretation, but several additional complexities have to be addressed when interpreting K–Ar age spectra as described in the following.

Firstly, all different K-bearing mineral phases which contribute to the age have to be identified, with possibly several inherited and several authigenic phases. Secondly, the effect of inherited K-bearing minerals from the host rock has to be estimated (e.g. Zwingmann et al. 2010), and thirdly, the possibility for fault reactivation and the generation of more than one phase of authigenic K-bearing minerals has to be taken into account (Torgersen et al., 2015a; Viola et al., 2016; Fossen et al., 2021).

5.1.1. K-bearing mineral phases

Our mineralogical dataset shows that the following K-bearing minerals can contribute to the K–Ar dates: K-feldspar (up to 20 wt% in some fractions), biotite (up to 65 wt% in some fractions), illite/muscovite (up to 22 wt% in some fractions), smectite (up to 100 wt% in some fractions), and zeolite (up to 14 wt% in some fractions). Biotite, illite/muscovite and K-feldspar have known average K-contents of 9 wt%, 6/

Table 1
Results from K–Ar fault gouge geochronology.

Sample	Sample locality (UTM 32)		Dip direction/ dip	Grain size fraction (μm)	^{40}Ar*				K			Age data	
	Easting	Northing			Mass mg	Mol/g	σ (%)	^{40}Ar* %	Mass mg	wt %	σ (%)	Age (Ma)	± σ (Ma)
VAH_53_3	347717	6869820	075/85	<0.1	2.284	6.254E-11	1.45	14.4	49.9	0.408	1.53	86.3	1.8
				0.1–0.4	2.302	9.577E-11	1.06	18.6	50.3	0.537	1.48	100.1	1.8
				0.4–2	1.624	2.028E-10	0.80	34.7	50.8	0.927	1.38	121.9	1.9
				2–6	2.084	2.679E-10	0.45	50.5	50.8	1.202	1.33	124.1	1.7
				6–10	1.622	2.818E-10	0.54	52.7	51.5	1.265	1.32	124.1	1.7
VAH_58	349682	6873671	122/55	<0.1	2.436	9.175E-11	0.92	28.2	50.2	0.672	1.44	77.1	1.3
				0.1–0.4	2.552	2.309E-10	0.42	57.9	50.4	1.208	1.33	107.0	1.5
				0.4–2	2.498	5.253E-10	0.31	85.6	51.5	1.857	1.25	156.1	1.9
				2–6	1.834	5.261E-10	0.37	90.0	51.4	1.605	1.28	179.7	2.3
				6–10	2.692	4.987E-10	0.30	91.5	49.7	1.427	1.31	191.1	2.4
VAH_116_1	286379	6856537	277/53	<0.1	1.082	1.832E-10	1.10	41.0	50.2	0.886	1.39	115.5	2.0
				0.1–0.4	2.504	4.845E-10	0.31	60.0	50.0	1.807	1.26	148.3	1.9
				0.4–2	1.978	7.797E-10	0.32	72.0	50.5	2.532	1.20	169.3	2.0
				2–6	1.196	7.407E-10	0.45	70.5	51.4	2.697	1.18	151.8	1.8
				6–10	1.686	7.139E-10	0.36	68.6	50.4	2.551	1.20	154.6	1.9
VAH_198	343457	6901544	122/80	<0.1	1.316	1.467E-09	0.39	72.0	50.2	4.458	1.10	180.4	2.0
				0.1–0.4	1.368	1.809E-09	0.37	77.6	50.1	4.595	1.09	213.9	2.3
				0.4–2	1.034	1.744E-09	0.46	77.6	50.3	4.318	1.10	219.0	2.5
				2–6	1.314	1.549E-09	0.39	77.4	50.7	4.197	1.11	201.2	2.2
				6–10	1.886	1.522E-09	0.31	77.9	49.7	4.278	1.11	194.3	2.1
VAH_250_2	385184	6863534	322/67	<0.1	1.548	1.002E-10	1.35	65.5	51.1	0.432	1.52	128.9	2.5
				0.1–0.4	2.182	2.400E-10	0.47	83.3	50.9	0.812	1.40	162.8	2.3
				0.4–2	1.144	6.577E-10	0.48	94.2	50.7	1.894	1.25	189.9	2.4
				2–6	1.796	9.386E-10	0.33	96.7	50.8	2.204	1.22	230.2	2.7
				6–10	1.588	9.876E-10	0.35	96.9	52.0	2.207	1.22	241.2	2.9
VAH_267_2	369092	6833464	261/65	<0.1									
				0.1–0.4	1.574	8.296E-11	1.57	60.6	35.9	0.290	1.66	157.9	3.5
				0.4–2	2.008	2.601E-10	0.47	81.0	52.3	0.662	1.43	213.4	3.0
				2–6	0.986	5.212E-10	0.59	89.0	50.4	1.221	1.33	230.7	3.2
				6–10	1.082	6.271E-10	0.51	89.3	50.5	1.410	1.31	239.9	3.1

10 wt% and 14 wt%, respectively (Barthelmy, 2014). Smectite and zeolite are generally considered not to contain K in their crystal structure (Howie et al., 1992). It is, however, common to find smectite intercalated with illite due to smectite illitization (Altaner and Ylagan, 1997), which can be difficult to identify with XRD analysis at low concentrations (Bense et al., 2014; Viola et al., 2016; Scheiber et al., 2019). For fractions consisting entirely of smectite, but giving a well-defined K–Ar date, we therefore assume that the K-content in these fractions can be assigned to illite interlayers in smectite.

5.1.2. The effect of inheritance

The gneisses of the WGR commonly contain K-feldspar, and this mineral is therefore an obvious candidate for inheritance in our samples. Dunlap and Fossen (1998) and Walsh et al. (2013) showed that the K-feldspar in the WGR cooled through ~400 °C at 400–330 Ma and through ~200 °C at 330–230 Ma. If a fraction consists solely of inherited K-feldspar, the K–Ar date should be the age at closure temperature (200–400 °C, Reiners et al. (2017)). Alternatively, K-feldspar might be an authigenic growth phase depending on fluid geochemistry and PT

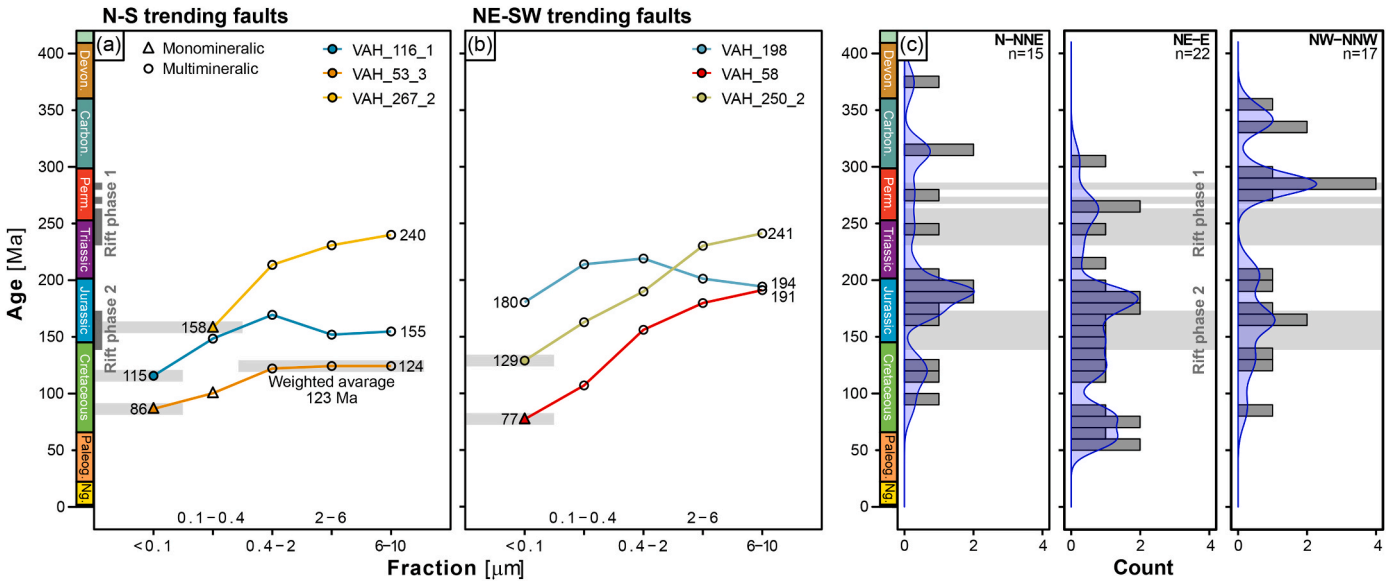

Fig. 8. K–Ar fault gouge data from (a) N–S striking faults and (b) NE-SW striking faults. Circles indicate fractions containing more than one K-bearing mineral phase while triangles indicate monomineralic fractions. Filled shapes and grey bars show interpreted ages of faulting events and maximum ages of faulting (see text for details). (c) Previously published K–Ar fault gouge ages from Western Norway containing both faulting events and maximum ages of faulting grouped by fault strike orientation (bin width 10 and Kernel distribution (bandwidth 10), modified from Fossen et al., 2021).

conditions during faulting (Brockamp and Clauer, 2013; Torgersen et al., 2015b). In this case, euhedral crystal growth might be expected. From BSE images, we see that the K-feldspars (at least in the coarsest fractions) in our samples do not show crystal faces, but are rather replaced by smectite or fractured and decomposed along edges, indicating that they might represent inherited grains. Finally, inherited K-feldspar might have isotopically re-equilibrated during faulting (Zwingmann et al., 2010), and might even show younger cooling ages than the actual timing of faulting if the faulting temperature was higher than the closure temperature of K-feldspar (Koehl et al., 2018).

Biotite is another candidate for inheritance and is abundant in sample VAH_198. Biotite is abundant in the host rock of this fault gouge, and it is therefore probable that at least some of the biotite is inherited. Earlier K–Ar biotite dating from within the study area showed cooling of biotite through 300 °C at about 340 Ma (Lux, 1985). K–Ar dating of biotite is, however, complicated (Kelley, 2002) and the interpretation of this age should be done with caution. If the biotite is inherited, we would expect to see the 340 Ma cooling age reflected in the K–Ar gouge data from the coarsest fraction. Authigenic formation of biotite in fault gouge has not been documented in the literature so far, but cannot be excluded depending on fluid chemistry and PT conditions during faulting.

Illite is commonly interpreted to represent an authigenic phase in fault gouges if located in crystalline and high-grade metamorphic rocks. Out of all the studied samples, VAH 267_2 appears to be the only one whose two coarsest fractions comprise 2M1 illite (Supplementary 6). Thus, we cannot rule out inheritance of host-rock muscovite. Muscovite is usually assumed to have an Ar closure temperature of ~350 °C (Harrison et al., 2009) and within the study area, muscovite ^{40}Ar–^{39}Ar ages are about 380–400 Ma (Chauvet and Dallmeyer, 1992; Walsh et al., 2013). If some inherited muscovite is present, we would expect to see the dates of the coarsest fractions to converge towards the muscovite cooling ages, potentially making the dates older than the actual faulting age. However, depending on the PT conditions of faulting, inherited muscovite might become isotopically reset during faulting (Zwingmann et al., 2010).

Smectite, like illite, is generally assumed to represent an authigenic phase in a gouge in magmatic or high-grade metamorphic host rocks, since it is a low-T mineral formed under diagenetic or hydrothermal processes (Reid-Soukup and Ulery, 2018).

Zeolite is a common product of low temperature (<250 °C) interaction between fluids and crustal rocks (Weisenberger and Bucher, 2010), and is therefore generally interpreted to represent an authigenic growth phase during low-temperature faulting. Zeolite has earlier been documented in fault zones in Norway (Tartaglia et al., 2020). Zeolites do commonly contain very little K, and we therefore assume the influence of zeolite on the K–Ar gouge dates to be minor.

5.1.3. *Fault reactivation*

Reactivation of a fault can potentially lead to several generations of authigenic illite/smectite growth, adding additional complexity to the already complex mixing between inherited and authigenic phases. Unravelling the contribution from inherited or partly re-equilibrated phases versus potentially several generations of authigenic phases is in many cases not unequivocally possible, and many K–Ar dates potentially represent mixed dates not representing any faulting event. We therefore in the following use a conservative approach, and state that some mixing cannot be ruled out even for the finest fractions.

5.1.4. *N–S striking faults*

5.1.4.1. VAH_116_1. In this sample, smectite, K-feldspar and illite/muscovite contribute to the K–Ar dates. The cracked and irregular K-feldspars partly replaced by smectite are interpreted to represent inherited grains from the host rock. The three coarser fractions that contain K-feldspar have similar mineralogical compositions and yield dates of 155 ± 2 Ma (6–10 µm), 152 ± 2 Ma (2–6 µm) and 169 ± 2 Ma (0.4–2 µm). These dates correspond mainly to K-feldspar and illite/muscovite in the samples, since those have a much higher K-content than smectite. Both K-feldspar and illite/muscovite might be either inherited from the host rock, (partially) reset or authigenic. We choose therefore not to attribute much significance to these dates. The two finer fractions contain smectite and illite/muscovite with dates of 148 ± 2 Ma (0.1–0.4 µm) and 115 ± 2 Ma (<0.1 µm). We interpret the date from the 0.1–0.4 µm fraction to result from mixed generations of authigenic illite and smectite, and the <0.1 µm fraction to reflect authigenic smectite with interlayered illite grown during faulting at 115 ± 2 Ma (Fig. 8a). Due to possible traces of illite/muscovite in this fraction, we consider this a maximum age of faulting.

5.1.4.2. VAH_53_3. In this sample, smectite and K-feldspar contribute to the K-content. Dates for the three coarser fractions are similar and plot around 123 ± 2 Ma. Earlier studies (e.g. Torgersen et al. 2015a, 2015b; Scheiber et al., 2019; Fossen et al., 2021) interpreted similar overlapping dates among fractions to represent an extensive faulting event. The K-content from smectite is minor compared to K-feldspar, indicating that the K-feldspar should have an important control on the resulting dates. BSE imaging (Fig. 7b) shows that K-feldspar in the 6–10 μm fraction gets replaced by smectite and does not show euhedral crystal shapes as expected if authigenic. That all three grain size fractions yielded identical ages within the age uncertainties, despite variable K-content, suggests that the K-feldspar was isotopically reset at c. 123 Ma, which we tentatively interpret as an earlier period of activity along this fault (Fig. 8a). Similar ages have been detected elsewhere in Western Norway (Fig. 8c, Supplementary 8) and it is also similar to the ca. 115 Ma faulting age from VAH_116 (see above). The two finer fractions contain only smectite, where we interpret the 0.1–0.4 μm fraction to be a mixed date rather than an individual faulting event and the youngest age of 86 ± 2 Ma (<0.1 μm) to represent an age of faulting (Fig. 8a).

5.1.4.3. VAH_267_2. VAH_267_2 did not yield an <0.1 μm fraction. The coarser fractions contain illite/muscovite, plagioclase and zeolite, whereas smectite is the only K-bearing mineral in the 0.1–0.4 μm fraction. The decreasing content of illite/muscovite with fraction size indicates that this might be an inherited muscovite component, which is further supported by the 2M1 illite in the coarsest fractions (Supplementary 6). We assume the K-contribution from plagioclase to be minor. The inherited muscovite, together with the inclined age spectrum indicates that the dates of the three coarser fractions represent mixed ages. We interpret the monomineralic finest fraction (0.1–0.4 μm) to represent authigenic smectite/illite growth during a faulting event at 158 ± 4 Ma (Fig. 8a).

5.1.5. NE–SW striking faults

5.1.5.1. VAH_198. In this sample, K-feldspar, biotite, zeolite and smectite are the K-bearing minerals contributing to the K–Ar dates. This sample has an unusual composition since it contains biotite in all fractions, with biotite content increasing towards smaller grain fractions. Biotite Ar cooling ages in the area are typically 400-380 Ma (Lux, 1985), which suggests that the biotite has to be at least partially reset or authigenic. K-feldspar is assumed to be inherited, as indicated by its fractured and craked appearance in BSE images of the 6–10 μm fraction (Fig. 6g). Based on the concave-up age spectrum and unusual mineralogy with uncertain proportions of inheritend and reset or authigenic biotite, the significance of any of the dates from this sample is uncertain (Fig. 8b).

5.1.5.2. VAH_58. In this sample, K-feldspar, smectite and potentially plagioclase are the only K-bearing minerals contributing to the K–Ar dates (Fig. 7e). From BSE images we see that the K-feldspar of the coarsest fraction is fractured, indicating an inherited origin. XRD analysis of VAH_58 shows that all fractions except the <0.1 μm fractions contain K-feldspar, and we assume these fractions to show mixed dates. The finest fraction (<0.1 μm), however, only contains smectite and we interpret the date of this fraction to represent authigenic smectite/illite growth during faulting at 77 ± 1 Ma (Fig. 8b).

5.1.5.3. VAH_250_2. In this sample, smectite, K-feldspar, potentially plagioclase and zeolite contribute to the K–Ar dates, where the amount of smectite increases and K-feldspar decreases with decreasing grain size (Fig. 7f). Together with BSE images showing K-feldspar replaced by smectite, this indicates that K-feldspar, at least partly, is inherited from the host rock. This indicates that all fractions containing both K-feldspar and smectite represent mixed dates, and even the finest fraction, which still contains ca. 6% K-feldspar, would be older than the main smectite growth event. However, assuming an inherited K-feldspar age of >240 Ma, and a minor K-contribution from smectite, the age of the authigenic smectite component would need to be unrealistically low to pull down the age of the finest fraction to 129 Ma. Therefore, we suspect that some of the K-feldspar in the finest fraction might be authigenic or reset, as also interpreted for a gouge sample of the Lærdal fault by Tartaglia et al. (2020). The presence of zeolite in the gouge indicates that temperatures during faulting could have been up to 250 °C, a temperature where K-feldspar can grow (e.g. Mark et al. 2008; Brockamp and Clauer 2013). The date of the finest fraction of 129 ± 3 Ma still needs to be regarded as a maximum age of faulting (Fig. 8b). The age overlaps with the 123 Ma age of sample VAH_53_3 (Fig. 8a) and with similar ages interpreted from other faults in the study area (Fig. 8c, Fossen et al., 2021).

5.2. Paleostress analysis

In an attempt to model the stress field(s) which led to the observed fault and fracture pattern in our study area, we performed paleostress analysis using the software WinTensor by Delvaux and Sperner (2003). To highlight different aspects of our data set, we applied two different approaches to sort and treat the structural data during paleostress analysis: 1) a station approach, and 2) a fault mineralization approach.

5.2.1. Station approach

The station approach is suited to show local variations and the potential effect of inheritance of trends from ductile precursor structures. We assigned our field measurements to 24 stations (Fig. 9). The measurements assigned to each station are located within less than 100 m distance from each other. The stations are colour-coded based on the relationship between brittle fracture and fault measurements and the main ductile foliation at that station (Fig. 9g): 1) if the measured fractures are mainly parallel to the foliation, the station is blue, 2) if the measured fractures mainly cut the foliation, the station is orange, and 3) if fractures are both parallel to and cutting the foliation, the station is red. In addition, grey stereoplot background indicates stations where faults and fractures are dominated by mica mineralizations and strained host rock (Fig. 9b–f). For each station, we conducted individual paleostress analyses (Fig. 9a–f). The resulting paleostress analyses show filled arrows (Fig. 9) for stress tensors derived from seven or more faults and fracture measurements, and for stress tensors with an average misfit angle (alpha) of 5° or less. Hollow arrows in Fig. 9 represent stress tensors derived from 5 to 6 fracture and fault measurements and an average misfit angle (alpha) higher than 5°, and are therefore considered less reliable. Details on these analyses and the mineralizations on fracture surfaces are found in the supplementary material (Supplementary 7).

A total of 24 local stress tensors with R' classification were inferred, whereof seven are extensional, seven are transtensional, five are transpressional, four are strike-slip, and one is compressional (Fig. 9). Of the six transpressional and compressional local stress tensors, all except one (station 11) include fractures and faults parallel to the foliation, and five local stress tensors are from stations with mica/stretched host rock mineralizations indicating the formation of these local stress tensors under relatively high temperatures. Subarea B is dominated by extension (Fig. 9b), subarea F is dominated by transpression (Fig. 9f), whereas the other subareas are not dominated by a spesific stress tensor (Fig. 9a, c-e). From the 22 local stress tensors where the extension direction (σ_3) is (sub)horizontal (excluding station 17 and 18), 14 have σ_3 plotting in the NW–SE sector and 7 have σ_3 plotting more or less E–W, whereas 3 have σ_3 plotting in the SW–NE sector.

5.2.2. Fault mineralization approach

The fault mineralization approach is suited to potentially unravel the relative timing of different paleostress fields, by modelling the local

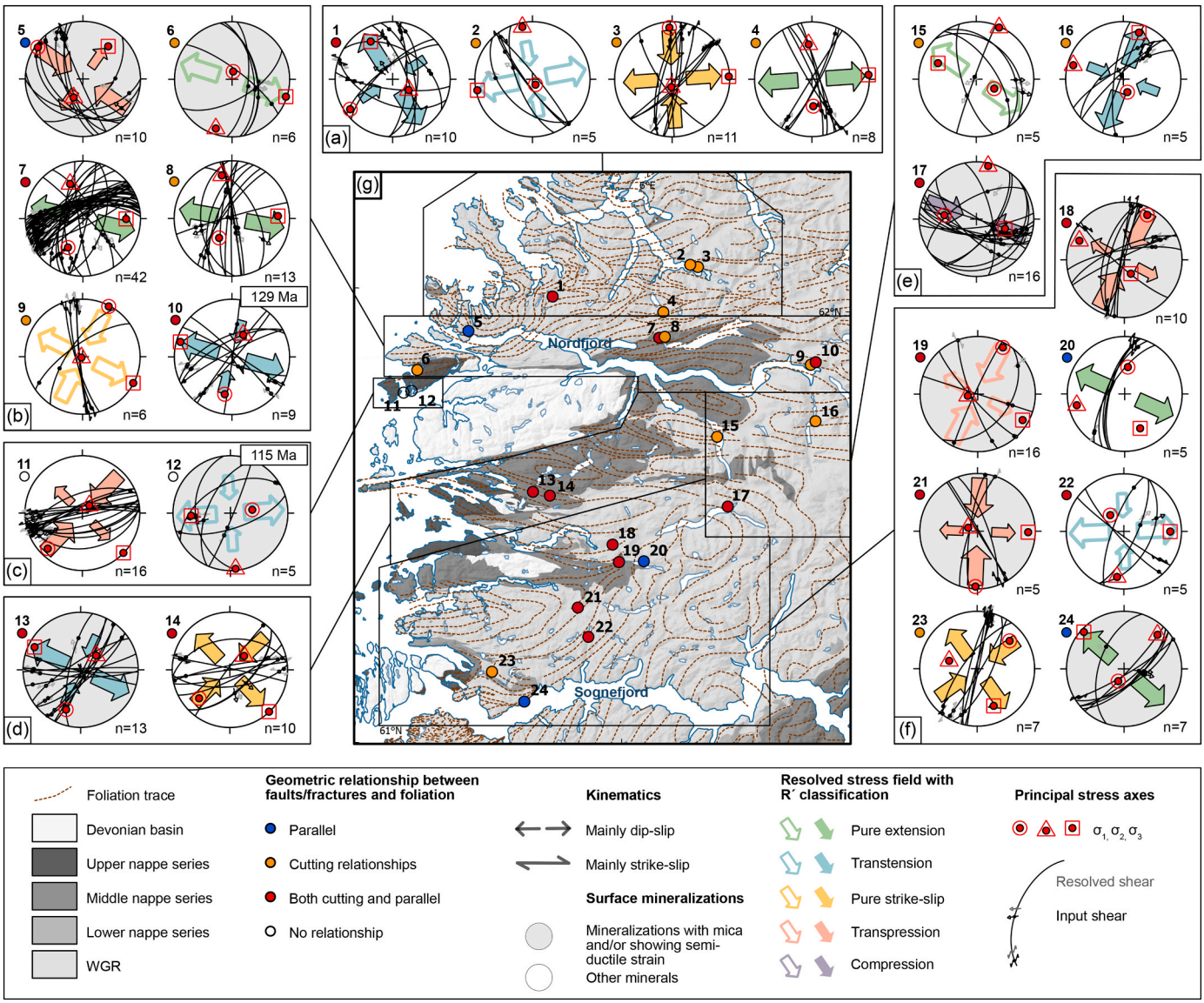

Fig. 9. (a–f) Results from paleostress analysis based on dividing the study area into 24 stations (station approach). (g) Tectonic map with foliation traces. Points mark the location of the station and colours indicate the relationship between foliation and fractures. Background arrows in stereoplots indicate the type of resolved stress field based on R′ classification (hollow arrows indicate local stress tensors with 5 to 6 surfaces included; filled arrows represent local stress tensors with 7 or more surfaces included, or local stress tensors with average misfit angle of 2–5° (supplementary 7)). (For interpretation of the references to colour in this figure legend, the reader is referred to the Web version of this article.)

stress tensors based on fault and fracture mineralization (Fig. 10). In this approach, it is assumed that higher temperature mineralizations such as mica and semi-ductile strained fracture surfaces formed earlier than lower-temperature mineralizations such as zeolite and calcite. This relationship is confirmed by the observation of zeolite and calcite mineralizations having crystallized on top of higher temperature epidote, chlorite and quartz mineralization. Slip lines are often not observed on zeolite and calcite, but rather on epidote, chlorite or quartz. The general absence of slip lines implies that zeolite and calcite mostly crystallized on fractures formed during earlier faulting, and kinematic indicators associated with these faults and fractures are derived from the earlier mineralizations. Therefore, the resulting local stress tensors do not indicate the stress field for the time of calcite formation, but rather indicate what surfaces were reactivated during the time of mineralization. Details on the resulting stress tensors can be found in the supplementary material (Supplementary 7).

Similar to the station approach, we chose local stations with sufficient measurements for each of the mineral groups to obtain a local stress tensor. Note that the measurements included within one station are from a slightly larger area (<2 km, within the same rock types) than for the station approach. Local stations containing high T mineralizations and semi-ductile features, such as SHR, fit into two main local stress tensors: an extensional stress tensor with NW–SE to WNW–ESE extension direction, and a compressional stress tensor with NW–SE compression direction (Fig. 10a). The local stations containing epidote, chlorite and quartz surfaces show three main trends: compressional stress tensor with NW–SE compression direction, transpressional stress tensor with NW-SE compression direction, and strike slip local stress tensors with NW–SE to E–W σ_3 direction (Fig. 10b). The local stations with zeolite measurements show strike-slip and extensional local stress tensors with WNW–ESE σ_3 direction (Fig. 10c).

5.3. Combining paleostress and geochronology

To correlate our fault gouge ages with the modelled paleostress regimes, we identified the local stress tensors to which the fault planes for

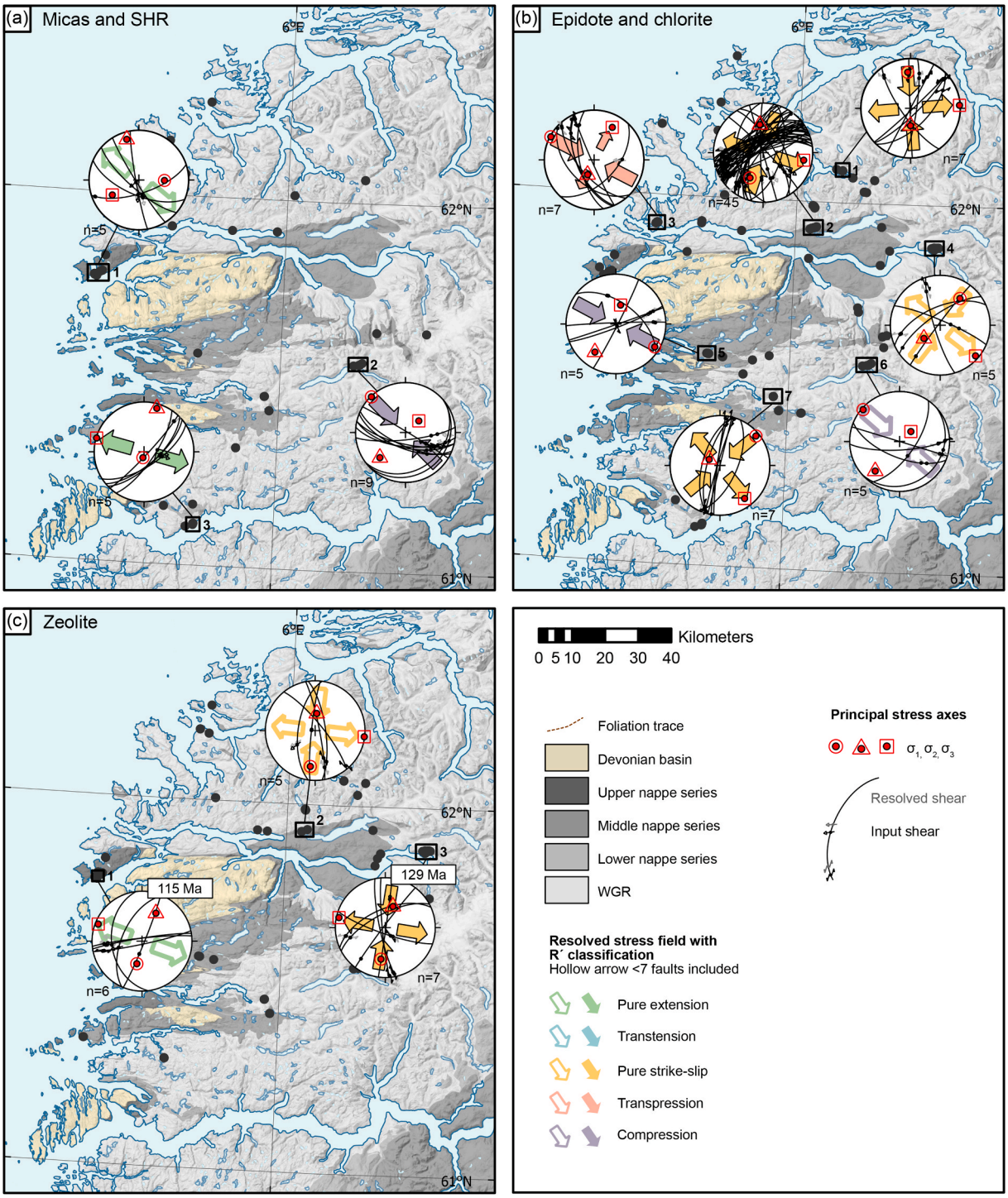

Fig. 10. Paleostress analysis based on fault and fracture mineralizations. Hollow arrows indicate local stress tensors with 5 to 6 surfaces included; filled arrows represent local stress tensors with 7 or more surfaces included, or local stress tensors with average misfit angle of 2–5° (supplementary 7). (a) Analysis of surfaces containing semi-ductile strained fracture and fault surfaces (SHR) and mica mineralization, some also together with chlorite, epidote, and/or quartz. (c) Analysis of surfaces containing chlorite and epidote mineralization, some also together with SHR and mica, zeolite and/or calcite. (d) Analysis of surfaces containing zeolite mineralization, some also together with chlorite, epidote, quartz, and/or calcite.

each dated fault were assigned in the two different paleostress approaches (Figs. 9 and 10). Note that the sense of slip observed on a fault's plane might not be directly related to the event of faulting which caused the authigenesis of the dated mineral phases. Only two of the dated faults fit into a local stress tensor, namely VAH_250_2 (maximum age of faulting 129 Ma) and VAH_116_1 (maximum age of faulting 115 Ma). In the station approach (Fig. 9), VAH_250_2 is represented in station 10, showing transtension with WNW–ESE σ_3 direction, whereas VAH_116 is included in station 12, showing transtension with E–W σ_3 direction. For the fault mineralization approach (Fig. 10) both VAH_250_2 and VAH_116_1 contain striated zeolite on the fault plane surface. VAH_250_2 is included in a stress tensor showing strike-slip with a WNW–ESE σ_3 direction (Fig. 10c), and VAH_116_1 in a local stress tensor showing extension with WNW–ESE σ_3 direction (Fig. 10c).

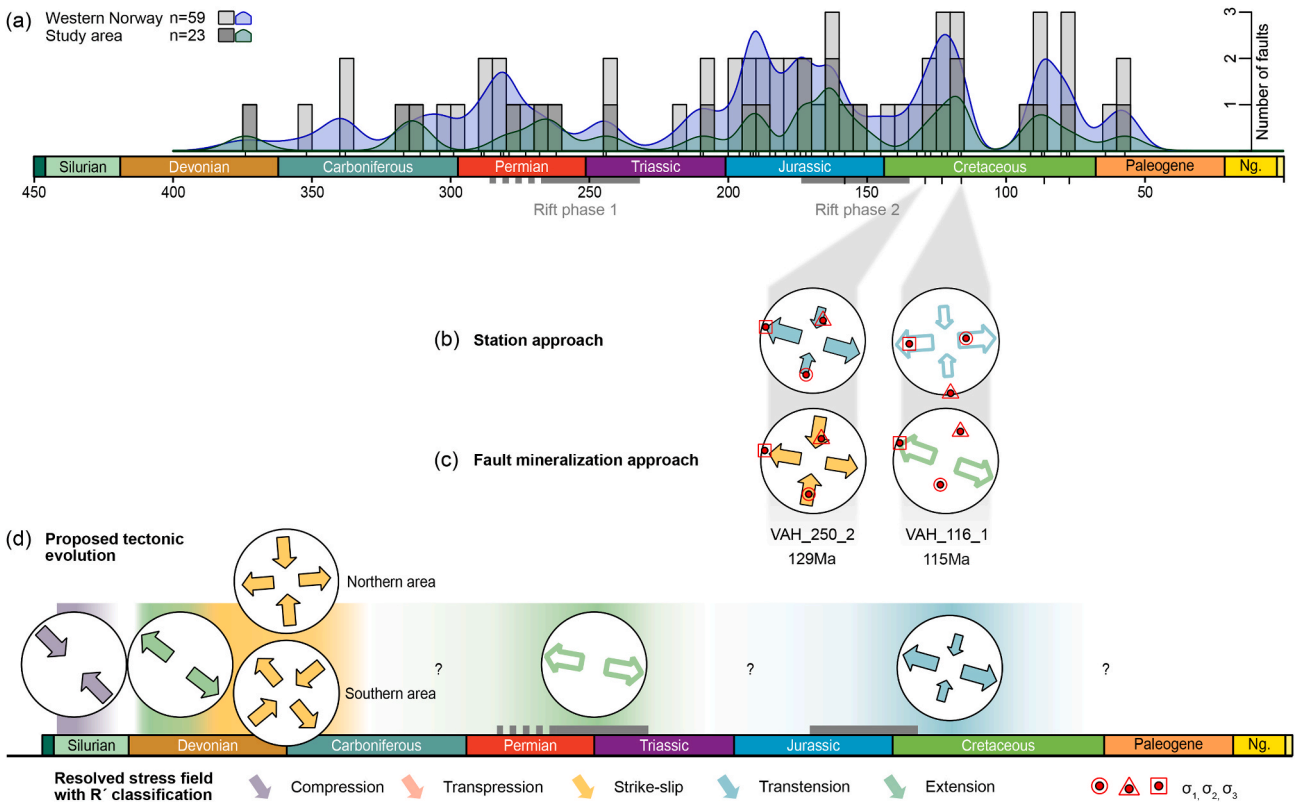

Fig. 11. (a) Histogram (bin width 5 and Kernel distribution (bandwidth 5) of K–Ar fault gouge ages from Western Norway that have been interpreted as constraining fault activity (modified after Fossen et al., 2021, Supplementary 8). Ages from previous studies outside the study area are shown in light grey bars and blue Kernel distributions, whereas ages from within the study area (own and existing data) are shown with dark grey bars and green kernel distribution. The probability density plots include both faulting event and maximum ages of faulting. (b–c) Correlation of fault gouge ages with two different approaches for paleostress analysis. (b) Station approach from Fig. 9 and (c) fault mineralization approach from Fig. 10. (e) Proposed tectonic evolution from Silurian to end-Cretaceous. (For interpretation of the references to colour in this figure legend, the reader is referred to the Web version of this article.)

Comparing these two approaches, it appears that they nicely match and complement each other. The local stress tensor implies that the local stress regime had a WNW–ESE σ_3 direction in the Early Cretaceous (129–115 Ma).

6. Reconstruction of the post-Caledonian brittle evolution

Our data set represents the first systematic investigation of brittle fault mineralizations between Sognefjorden and the Møre Margin (Fig. 1), allowing us to establish relative timing based on formation conditions of the different mineralizations. In the following, we first discuss the relative timing of the lineament and fracture networks, followed by the brittle evolution of the study area from pre-Devonian times to the Cretaceous. Here, we integrate the results from our lineament mapping, fault mineralization mapping, K–Ar dating and paleostress analysis with information from the literature.

6.1. Nature and relative age of fracture networks

From lineament studies and field data of fractures and faults, we detected two major trends in the fracture network striking N–S and NE–SW, and two minor trends striking NW–SE and E–W (Fig. 3b and c). The NE–SW-striking fractures and faults represent a dominating lineament- and fracture set in the study area (Fig. 3b and c) and their strike is in many places parallel or subparallel to the ductile foliation related to the NDSZ, NSZ and MTFC (Figs. 2 and 3). In metamorphic terranes, it is commonly known that brittle structures often develop by geometrically following planar ductile discontinuities in the bedrock (e.g. Butler et al. 2008; Massironi et al. 2011; Williams et al. 2019). We do, however, also observe extensive NE–SW-striking fractures and faults in the Bremanger granodioritic complex (Fig. 3, subarea C). Since the Bremanger granodiorite lacks any ductile deformation features, these faults must have either formed as a continuation of the (inherited) structures outside the granodiorite or they formed according to the given stress field affecting the isotropic granodiorite body. Similarly to the NE–SW fractures and faults discussed above, the E–W trending fractures and faults follow ductile precursors in several subareas (Figs. 2 and 3).

The N–S trending fractures and faults in contrast seem to represent a newly formed conjugate set, without any ductile precursor (Figs. 2 and 3). These N–S fractures and faults are dominant in most subareas (Fig. 3b), and N–S striking lineaments are often related to large-scale valleys, particularly in the inner Nordfjord area (Fig. 2, subarea E). These N–S striking lineaments have earlier been shown to be the most dominant lineament feature, both mainland and offshore Norway (e.g. Gabrielsen et al. 2002). The origin of this important fracture and fault trend has been debated. It has been speculated that these features follow long-lived Proterozoic zones of weakness (Gabrielsen et al., 2018). However, most of the N–S features cut the earlier ductile Caledonian foliation, and do not seem to follow any older shear belts. Several of the main N–S striking fault zones (e.g., Votedalen) formed within late Sveconorwegian intrusions (980–930 Ma; Wang et al., 2021) with only weak ductile Caledonian overprint, supporting a post-Caledonian origin for these N–S trending brittle features.

Our K–Ar fault gouge geochronology from the N–S trending faults indicates faulting activity during the Jurassic to Cretaceous ca. 158, 123–115 and 86 Ma (Fig. 8a). Other K–Ar gouge ages from Western Norway indicate that some of these N–S striking faults were also active earlier, in Devonian, Carboniferous and Permian-Triassic times, but

mostly during the Jurassic (Fig. 8c, Ksienzyk et al., 2016; Scheiber and Viola, 2018; Fossen et al., 2021). These studies often relate the N–S structural trend to rift structures formed during E–W extension (e.g. Fossen et al., 2017; Gabrielsen et al., 2018). Offshore, similar observations have been made, where N–S striking extensional structures formed during the rifting in the northern North Sea (e.g. Bartholomew et al. 1993; Doré et al. 1997; Reeve et al. 2015).

Interestingly, the majority of N–S striking faults and fractures in our data set does not show dip-slip movement as inferred from onshore and offshore interpretations but is rather dominated by strike-slip kinematics (Fig. 2). If these N–S striking fractures and faults originally formed during E–W extension as inferred during earlier studies, the faults must have been reactivated at a later stage creating the strike-slip kinematics. We interpret this as rather unlikely for the following reasons: very few fractures and faults having this orientation show dip-slip kinematics, the strike-slip kinematics are found throughout the region, and the faults and fractures have mostly subvertical dips, which is atypical for dip-slip faults. The N–S fractures and faults are therefore interpreted to have mostly been formed well before the Jurassic rifting episode, possibly as early as the Late Devonian-early Carboniferous (Fig. 11d). In the following, we will attempt to reconstruct the post-Caledonian brittle evolution based on previous work, the fault mineralization approach and the dated K–Ar fault gouges.

6.2. Silurian to Early-Devonian (Caledonian) compression

The probably oldest mineralizations are represented by stretched micas and/or semi-ductile strained host rock minerals, often together with epidote/chlorite/quartz, indicating relatively high temperature during formation. From the station approach, five out of six stations with compressional or transpressional local stress tensors contain such surfaces (Fig. 9), indicating that at least some of these structures might have formed during Caledonian compression/transpression (Fig. 11d). Similar compressional local stress tensors are found in the fault mineralization approach (Fig. 10a and b). Compressional stress fields have been recorded from the ca. 460 Ma Rolvsnes granodiorite on Bømlo further south (Scheiber et al., 2016). There, stretched mica revealed ^{40}Ar–^{39}Ar-dates of ca. 450 Ma formed under a NNW–SSE transpressional stress field, whereas faults related to dykes intruding at 435 Ma formed under WNW–ESE shortening. Caledonian compression was probably ongoing in our region until a switch to syn- and post-collisional extension occurred at around 400 Ma (Fossen, 2010).

6.3. Middle to Late Devonian NW–SE extension in an overall transtensional system

Apart from the compressional local stress tensors, high-T mineralizations also fit into ENE–WSW to NW–SE extensional/transtensional local stress tensors (Figs. 9 and 10a). These features could be early post-Caledonian structures formed in the Middle to Late Devonian, around 400–370 Ma, when rocks passed through the muscovite closure temperature in the region, as interpreted by Walsh et al. (2013). NW–SE extension and brittle faulting in Early to Middle Devonian has been described from the Bergen area (Fossen and Dunlap, 1998; Larsen et al., 2003) and further south (Scheiber and Viola, 2018). The NW–SE extensional stress field is in accordance with early post-Caledonian penetrative ductile extension which was generally oriented towards the NW (mode I back-sliding, Fossen, 1992, 2010). The penetrative ductile extension was followed by a more localized (mode II) extension focused on large-scale shear zones, equally with top-NW shear sense in the south (Hardangerfjord shear zone, Jotun Detachment, Fossen, 1992; 2010). However, in our study area, the ductile extension direction is oriented towards the W along the NSD and top-to-the-WSW along the sinistral MTFZ (Fossen, 1992, 2010; Seranne, 1992; Osmundsen and Andersen, 2001), interpreted to be the result of a large-scale transtensional system in the Middle to Late Devonian (Krabbendam and Dewey, 1998). In such a transtensional system, our derived NW–SE extensional stress field could be explained as representing the orthogonal stretching direction in a strain-partitioned system, with the strike-slip component taken up along strands of the MTFZ (Krabbendam and Dewey, 1998).

6.4. Late Devonian to early Carboniferous strike-slip

Fractures and faults coated with epidote, chlorite, and quartz are the most common in the region (Fig. 4). These minerals form under a wide range of temperatures of ca. 400–100 °C (e.g. Bird and Spieler 2004; Inoue et al. 2009). Given the relatively slow cooling of the entire region (Dunlap and Fossen, 1998; Ksienzyk et al., 2014; Scheiber et al., 2016), the area stayed at temperatures of ca. 400–100 °C from the Devonian until at least the beginning of the Mesozoic, and fractures and faults containing these mineralizations could therefore have formed and/or could have been reactivated during a long time span. In Western Norway, faults containing similar mineralizations have been interpreted to have formed and been reactivated from the Late Devonian-early Carboniferous to the Permian, with possible Mesozoic reactivation (e.g. Braathen, 1999; Larsen et al., 2003; Walsh et al., 2013).

The most prominent local stress tensors obtained from the fault mineralization approach represent strike-slip regimes (R' = 1.43–1.75) with a E–W to NW–SE σ_3 direction and a N–S to NE–SW σ_1 direction (Fig. 10b). Based on paleocurrent and structural analysis of the Devonian Kvamshesten basin, Osmundsen et al. (1998) proposed a model where NW–SE extension and perpendicular NE–SW shortening was overprinted by younger W–E extension and perpendicular N–S shortening from the Middle Devonian to the early Carboniferous, indicating two independent stress fields through time, with the σ_3 direction rotating anticlockwise from NW to W through time. Alternatively, Osmundsen and Andersen (2001) proposed a model where the change in orientation of the extension and shortening directions mainly depends on the distance from the MTFZ, similar to the strain-partitioned transtensional model proposed by Krabbendam and Dewey (1998). From the fault mineralization approach (Fig. 10b), we see that the σ_3 orientation turns into an E–W trend when approaching the MTFC, whereas the stations towards Sognefjorden in the south show a tendency to a NW–SE trending σ_3. The same trends are partially reflected in the station approach (Fig. 9), which indicates a changing stressfield depending on the distance from the MTFC in Late Devonian and early Carboniferous, as proposed by Osmundsen and Andersen (2001) (Fig. 11d).

6.5. Permian E–W extension (rift phase 1)

A few E–W pure extensional local stress tensors are present in the station approach. These local stress tensors are dominated by fractures striking N–S and NE–SW showing normal dip-slip to oblique-slip kinematics. Similar approximately E–W to ENE–WSW extensional stress fields are well known from SW Norway and along the Møre margin, and have earlier been interpreted to first initiate in the Permian and Early Triassic during rift phase 1 (e.g. Torsvik et al., 1997; Fossen and Dunlap, 1998; Walsh et al., 2013; Fossen et al., 2017; Theissen-Krah et al., 2017; Scheiber and Viola, 2018). The W-plunging Dalsfjord fault (Eide et al., 1994) shows Permian ages from palaeomagnetic and ^{40}Ar–^{39}Ar dating, and K–Ar fault gouge ages from Western Norway show a peak of activity in the early to mid Permian (Ksienzyk et al., 2016; Viola et al., 2016; Scheiber et al., 2019; Fossen et al., 2021) (Figs. 8c and 12a). Interestingly, this elsewhere important phase does not seem to be very prominent in our data set. Only few measurements fit into such purely extensional E–W stress fields in the station approach, none in the fault mineralization approach (Figs. 9 and 10), and none of our K–Ar gouge dates are present from this time span (Fig. 8).

6.6. Late Jurassic to Late Cretaceous WNW–ESE transtension

All our four monomineralic K–Ar fault gouge ages, the tentative

faulting age of 123 Ma and the two maximum ages of faulting fall into the Late Jurassic to Late Cretaceous (Figs. 8 and 11). Five of the six ages post-date the well-known Middle Jurassic to Early Cretaceous rift phase 2 (Fig. 11a; Gabrielsen et al., 1999; Viola et al., 2016; Fossen et al., 2017). Rift phase 2 probably represents crustal stretching, but the orientation of the stress field during this phase is debated, from NW–SE or E–W extension (e.g. Bartholomew et al., 1993; Færseth, 1996; Færseth et al., 1997; Reeve et al., 2015), or rotation from E–W extension to NW–SE extension to NE–SW extension (e.g. Doré et al., 1997; Davies et al., 2001). Our oldest sample VAH_267_2 (158 Ma), associated with zeolite mineralization, does not fit into any of the local stress tensors from the fault mineralization approach (Fig. 10). However, the clear strike-slip kinematics of the fault (subhorizontal slip lines) indicates that this fault is not a typical dip-slip rift-related structure.

The five younger ages overlap with what seems to be two regional faulting events when combined with K–Ar fault gouge ages documented onshore by others at around 130–110 Ma (Ksienzyk et al., 2016; Viola et al., 2016; Scheiber and Viola, 2018; Tartaglia et al., 2020; Fossen et al., 2021) and 90–70 Ma (Scheiber et al., 2019; Tartaglia et al., 2020; Fossen et al., 2021) (Fig. 11a). These Cretaceous faulting events have been interpreted as a response to hyperextension along the Mid-Norwegian margin, resulting in cooling and exhumation of the onshore area (Fossen et al., 2017; Ksienzyk et al., 2016; Viola et al., 2016; Scheiber and Viola, 2018; Tartaglia et al., 2020) and coincide with two periods of suggested tectonic activity in the Norwegian Sea (Færseth and Trond, 2002; Theissen-Krah et al., 2017). Two of the dated gouges, VAH_250_2 and VAH_116_1, show kinematics with a E–W to WNW–ESE trending σ_3 and extensional to strike-slip stress tensors. The kinematics and resulting stress tensor could be partly inherited from the previous strike-slip stress tensor derived from epidote-chlorite-quartz mineralizations, but since some of the dated faults also contain striated zeolite and calcite, we interpret the derived local stress tensor to represent the prevailing stress condition during the Cretaceous (Fig. 11d).

The VAH_267_2 (158 Ma) and VAH_116_1 (115 Ma) faults contain synkinematic zeolites, indicating that the widespread low-T zeolite mineralizations could be primarily of Late Jurassic to Cretaceous age. Similarly, the VAH_53_3 fault (123 and 86 Ma) contains striated calcite, supporting the field observation that calcite mineralizations generally are younger than the zeolite mineralizations, possibly being of mainly Cretaceous age, in accordance with the interpretation of Watts (2001).

7. Summary and conclusions

Our interpretation of brittle fault mineralizations, K–Ar fault gouge data and paleostress analyses reveal the following brittle evolution for the area between Sognefjorden and the Møre Margin (Fig. 12e):

(1) High-T fault surface minerals indicate NW–SE compression in the Late Silurian to Early Devonian, followed by NW–SE extension under semi-ductile conditions.
(2) Epidote-, chlorite- and quartz-bearing fractures and faults are interpreted to have initiated mainly in the Middle Devonian to early Carboniferous, representing two distinct paleostress fields: (1) NW–SE compression and, (2) strike-slip stress regimes with a changing σ_3 direction from NW–SE in the southern part of the region to E–W in the northern part of the region. The changing stress tensor is interpreted to be due to increasing strain partitioning closer to the MTFC.
(3) Only a limited number of epidote-, chlorite- and quartz-bearing fractures and faults fit into purely E–W extensional local stress regimes, and these could probably be related to rift phase 1 in the Permian to Early Triassic in the North Sea, though this phase seems not to be very prominent in our study area.
(4) All four K–Ar fault gouge ages and the two maximum ages of faulting fall into the Late Jurassic to Cretaceous, with only one age overlapping with the well-known Late Jurassic offshore rift phase 2. The other five ages constrain two younger extensive faulting events under a WNW–ESE transtensional stress regime with related fluid flow and precipitation of zeolite and calcite in Middle (123–115 Ma) and Late (86–77 Ma) Cretaceous times. These two faulting events can be related to periods of increased tectonic activity in the Norwegian Sea.

Our results show that the brittle architecture of the northern section of the passive margin of Western Norway is controlled by two dominant brittle precursor directions (NE–SW and E–W striking shear zones) as well as two newly formed, mainly strike-slip fault sets with conjugate orientations to the brittle precursors (N–S and NW–SE striking). The interpreted Late Devonian to early Carboniferous age of the N–S trending lineaments is different from previous models where the important N–S lineament population in Western Norway was interpreted to have mainly originated during Permo-Triassic or Jurassic E–W rifting. The domination of strike-slip fault sets is different from the mainly dip-slip controlled brittle architecture of the southern section of the passive margin south of Sognefjorden, indicating a more prominent transtensional/strike-slip regime from the Late Devonian onwards at the transition to the Møre margin. Our multi-method approach shows that detailed fault mineralization mapping is crucial for unravelling both kinematics and relative timing of brittle faulting, giving, combined with paleostress analysis, a more complete picture of the brittle evolution of the area than K–Ar fault gouge geochronology alone.

Author statement

Åse Hestnes: Conceptualization, Writing - Original Draft, Visualization, Formal analysis, Investigation. **Deta Gasser:** Conceptualization, Funding acquisition, Writing - Original Draft, Supervision, Investigation. **Thomas Scheiber:** Conceptualization, Funding acquisition, Writing - Review & Editing, Supervision, Investigation. **Joachim Jacobs:** Conceptualization, Funding acquisition, Writing - Review & Editing, Supervision, Investigation, Project administration. **Roelant van der Lelij:** Writing - Review & Editing, Formal analysis, Resources. **Jasmin Schönenberger:** Writing - Review & Editing, Formal analysis. **Anna Ksienzyk:** Writing - Review & Editing.

Funding

This work was funded by VISTA, a basic research programme in collaboration between The Norwegian Academy of Science and Letters and Equinor (grant number 6274).

Declaration of competing interest

The authors declare the following financial interests/personal relationships which may be considered as potential competing interests:
Åse Hestnes reports financial support was provided by VISTA.

Acknowledgements/Funding

We are grateful for thorough reviews by José L. Simón and Sam Haines, which improved the manuscript greatly. We thank Espen Torgersen and Tim Redfield for providing us with vertical derivative maps based on DTMs for lineament analysis. Irene Heggstad at UiB helped with imaging.

Appendix A. Supplementary data

Supplementary data to this article can be found online at https://doi.org/10.1016/j.jsg.2022.104621.

References

Altaner, S.P., Ylagan, R.F., 1997. Comparison of structural models of mixed-layer illite/smectite and reaction mechanisms of smectite illitization. Clay Clay Miner. 45, 517–533. https://doi.org/10.1346/CCMN.1997.0450404.

Andersen, T.B., Torsvik, T.H., Eide, E.A., Osmundsen, P.T., Faleide, J.I., 1999. Permian and Mesozoic extensional faulting within the Caledonides of central south Norway. J. Geol. Soc. 156, 1073–1080. London.

Angelier, J., 1984. Tectonic analysis of fault slip data sets. J. Geophys. Res. Solid Earth 89, 5835–5848. https://doi.org/10.1029/JB089iB07p05835.

Angelier, J., 1979. Determination of the mean principal directions of stresses for a given fault population. Tectonophysics 56. https://doi.org/10.1016/0040-1951(79)90081-7.

Barthelmy, D., 2014. Webmineral [WWW document]. http://webmineral.com/ accessed 12.17.21.

Bartholomew, I.D., Peters, J.M., Powell, C.M., 1993. Regional structural evolution of the North Sea: oblique slip and the reactivation of basement lineaments. In: Petroleum Geology Conference Proceedings, 4, pp. 1109–1122. https://doi.org/10.1144/0041109.

Bense, F.A., Wemmer, K., Löbens, S., Siegesmund, S., 2014. Fault gouge analyses: K-Ar illite dating, clay mineralogy and tectonic significance-a study from the Sierras Pampeanas, Argentina. Int. J. Earth Sci. 103, 189–218. https://doi.org/10.1007/s00531-013-0956-7.

Bird, D.K., Spieler, A.R., 2004. Epidote in geothermal systems. Rev. Mineral. Geochem. 56, 235–300. https://doi.org/10.2138/gsrmg.56.1.235.

Braathen, A., 1999. Kinematics of post-Caledonian polyphase brittle faulting in the Sunnfjord region, western Norway. Tectonophysics 302, 99–121. https://doi.org/10.1016/S0040-1951(98)00281-9.

Braathen, A., Osmundsen, P.T., Gabrielsen, R.H., 2004. Dynamic development of fault rocks in a crustal-scale detachment: an example from western Norway. Tectonics 23, 1–21. https://doi.org/10.1029/2003TC001558.

Brockamp, O., Clauer, N., 2013. Hydrothermal and unexpected diagenetic alteration in Permian shales of the Lodève epigenetic U-deposit of southern France, traced by K-Ar illite and K-feldspar dating. Chem. Geol. 357, 18–28. https://doi.org/10.1016/j.chemgeo.2013.08.009.

Butler, R.W.H., Bond, C.E., Shipton, Z.K., Jones, R.R., Casey, M., 2008. Fabric anisotropy controls faulting in the continental crust. J. Geol. Soc. 165, 449–452. https://doi.org/10.1144/0016-76492007-129.

Chauvet, A., Dallmeyer, R.D., 1992. 40Ar/39Ar mineral dates related to Devonian extension in the southwestern Scandinavian Caledonides. Tectonophysics 210, 155–177. https://doi.org/10.1016/0040-1951(92)90133-Q.

Corfu, F., Andersen, T.B., 2002. U–Pb ages of the Dalsfjord Complex, SW Norway, and their bearing on the correlation of allochthonous crystalline segments of the Scandinavian Caledonides. Int. J. Earth Sci. 91, 955–963. https://doi.org/10.1007/s00531-002-0298-3.

Corfu, F., Andersen, T.B., Gasser, D., 2014. The Scandinavian Caledonides: main features, conceptual advances and critical questions, 390. Geological Society, London, Special Publications, pp. 9–43. https://doi.org/10.1144/SP390.25.

Davies, R.J., Turner, J.D., Underhill, J.R., 2001. Sequential dip-slip fault movement during rifting: a new model for the evolution of the Jurassic trilete North sea rift system. Petrol. Geosci. 7, 371–388. https://doi.org/10.1144/petgeo.7.4.371.

Delvaux, D., Sperner, B., 2003. New Aspects of Tectonic Stress Inversion with Reference to the TENSOR Program, 212. Geological Society Special Publication, pp. 75–100. https://doi.org/10.1144/GSL.SP.2003.212.01.06.

Doré, A.G., Lundin, E.R., Fichler, C., Olesen, O., 1997. Patterns of basement structure and reactivation along the NE Atlantic margin. J. Geol. Soc. 154, 85–92. https://doi.org/10.1144/gsjgs.154.1.0085.

Dunlap, W.J., Fossen, H., 1998. Early Paleozoic orogenic collapse, tectonic stability, and late Paleozoic continental rifting revealed through thermochronology of K-felsdspars, souther Norway. Tectonics 17, 604–620.

Eide, E.A., Torsvik, T.H., Andersen, T.B., 1994. Absolute dating of brittle fault movements: late Permian and late Jurassic extensional fault breccias in western Norway. Terra 9, 135–139. https://doi.org/10.1046/j.1365-3121.1997.d01-21.x.

Færseth, R.B., 1996. Interaction of permo-triassic and jurassic extensional fault-blocks during the development of the northern North Sea. J. Geol. Soc. 153, 931–944. https://doi.org/10.1144/gsjgs.153.6.0931.

Færseth, R.B., Knudsen, B.E., Liljedahl, T., Midbøe, P.S., Søderstrøm, B., 1997. Oblique rifting and sequential faulting in the Jurassic development of the northern North Sea. J. Struct. Geol. 19, 1285–1302. https://doi.org/10.1016/s0191-8141(97)00045-x.

Færseth, R.B., Trond, L., 2002. Cretaceous evolution in the Norwegian Sea - a period characterized by tectonic quiescence. Mar. Petrol. Geol. 19, 1005–1027. https://doi.org/10.1016/S0264-8172(02)00112-5.

Fossen, H., 2010. Extensional Tectonics in the North Atlantic Caledonides: a Regional View, 335. Geological Society Special Publication, pp. 767–793. https://doi.org/10.1144/SP335.31.

Fossen, H., 1992. The role of extensional tectonics in the Caledonides of south Norway. J. Struct. Geol. 14, 1033–1046. https://doi.org/10.1016/0191-8141(92)90034-T.

Fossen, H., Dunlap, W.J., 1998. Timing and kinematics of Caledonian thrusting and extensional collapse, southern Norway: evidence from 40Ar/39Ar thermochronology. J. Struct. Geol. 20, 765–781. https://doi.org/10.1016/S0191-8141(98)00007-8.

Fossen, H., Khani, H.F., Faleide, J.I., Ksienzyk, A.K., Dunlap, W.J., 2017. Post-Caledonian extension in the West Norway–northern North Sea region: the role of structural inheritance. Geological Society, London, Special Publications 439, 465–486. https://doi.org/10.1144/SP439.6.

Fossen, H., Ksienzyk, A.K., Rotevatn, A., Bauck, M.S., Wemmer, K., 2021. From widespread faulting to localised rifting: evidence from K-Ar fault gouge dates from the Norwegian North Sea rift shoulder. Basin Research bre 12541. https://doi.org/10.1111/bre.12541.

Furnes, H., Skjerlie, K.P., Pedersen, R.B., Andersen, T.B., Stillman, C.J., Suthren, R.J., Tysseland, M., Garmann, L.B., 1990. The Solund—Stavfjord Ophiolite Complex and associated rocks, west Norwegian Caledonides: geology, geochemistry and tectonic environment. Geol. Mag. 127, 209–224. https://doi.org/10.1017/S0016756800014497.

Gabrielsen, R.H., Braathen, A., Dehis, J., Roberts, D., 2002. Tectonic lineaments of Norway. Nor. Geol. Tidsskr. 82, 153–174.

Gabrielsen, R.H., Nystuen, J.P., Olesen, O., 2018. Fault distribution in the precambrian basement of south Norway. J. Struct. Geol. 108, 269–289. https://doi.org/10.1016/j.jsg.2017.06.006.

Gabrielsen, R.H., Odinsen, T., Grunnaleite, I., 1999. Structuring of the northern Viking Graben and the Møre basin; the influence of basement structural grain, and the particular role of the Møre-Trøndelag Fault complex. Mar. Petrol. Geol. 16, 443–465. https://doi.org/10.1016/S0264-8172(99)00006-9.

Gómez, M., Vergés, J., Fernàndez, M., Torne, M., Ayala, C., Wheeler, W., Karpuz, R., 2004. Extensional geometry of the mid Norwegian margin before early tertiary continental breakup. Mar. Petrol. Geol. 21, 177–194. https://doi.org/10.1016/j.marpetgeo.2003.11.017.

Grathoff, G.H., Moore, D.M., 1996. Illite polytype quantification using WILDFIRE© Calculated X-ray diffraction patterns. Clay Clay Miner. 44, 835–842. https://doi.org/10.1346/CCMN.1996.0440615.

Grunnaleite, I., Gabrielsen, R.H., 1995. Structure of the Møre basin, mid-Norway continental margin. Tectonophysics 252, 221–251. https://doi.org/10.1016/0040-1951(95)00095-X.

Hacker, B.R., Andersen, T.B., Johnston, S., Kylander-Clark, A.R.C.C., Peterman, E.M., Walsh, E.O., Young, D., 2010. High-temperature deformation during continental-margin subduction & exhumation: the ultrahigh-pressure Western Gneiss Region of Norway. Tectonophysics 480, 149–171. https://doi.org/10.1016/j.tecto.2009.08.012.

Hacker, B.R., Andersen, T.B., Root, D.B., Mehl, L., Mattinson, J.M., Wooden, J.L., 2003. Exhumation of high-pressure rocks beneath the Solund basin, western gneiss region of Norway. J. Metamorph. Geol. 21, 613–629. https://doi.org/10.1046/j.1525-1314.2003.00468.x.

Hacker, B.R., Gans, P.B., 2005. Continental collisions and the creation of ultrahigh-pressure terranes: petrology and thermochronology of nappes in the central Scandinavian Caledonides. Bull. Geol. Soc. Am. 117, 117–134. https://doi.org/10.1130/B25549.1.

Hansen, J., Skjerlie, K.P., Pedersen, R.B., De La Rosa, J., 2002. Crustal melting in the lower parts of island acrs: an example from the Bremanger Granitoid Complex, West Norwegian Caledonides. Contrib. Mineral. Petrol. 143, 316–335. https://doi.org/10.1007/s00410-001-0342-5.

Harrison, T.M., Célérier, J., Aikman, A.B., Hermann, J., Heizler, M.T., 2009. Diffusion of 40Ar in muscovite. Geochem. Cosmochim. Acta 73, 1039–1051. https://doi.org/10.1016/j.gca.2008.09.038.

Howie, R.A., Zussman, J., Deer, W., 1992. An Introduction to the Rock-Forming Minerals. Longman London, UK.

Inoue, A., Meunier, A., Patrier-Mas, P., Rigault, C., Beaufort, D., Vieillard, P., 2009. Application of chemical geothermometry to low-temperature trioctahedral chlorites. Clay Clay Miner. 57, 371–382. https://doi.org/10.1346/CCMN.2009.0570309.

Kelley, S., 2002. Excess argon in K-Ar and Ar-Ar geochronology. Chem. Geol. 188, 1–22. https://doi.org/10.1016/S0009-2541(02)00064-5.

Koehl, J.P., Bergh, S.G., Wemmer, K., 2018. Neoproterozoic and Post-caledonian Exhumation and Shallow Faulting in NW Finnmark from K – Ar Dating and P/T Analysis of Fault Rocks, pp. 923–951.

Krabbendam, M., Dewey, J.F., 1998. Exhumation of UHP Rocks by Transtension in the Western Gneiss Region, Scandinavian Caledonides, 135. Geological Society Special Publication, pp. 159–181. https://doi.org/10.1144/GSL.SP.1998.135.01.11.

Ksienzyk, A.K., Dunkl, I., Jacobs, J., Fossen, H., Kohlmann, F., 2014. From orogen to passive margin: constraints from fission track and (U–Th)/He analyses on Mesozoic uplift and fault reactivation in SW Norway. Geological Society, London, Special Publications 390, 679–702. https://doi.org/10.1144/SP390.27.

Ksienzyk, A.K., Wemmer, K., Jacobs, J., Fossen, H., Schomberg, A.C., Süssenberger, A., Lünsdorf, N.K., Bastesen, E., 2016. Post-caledonian brittle deformation in the Bergen area, West Norway: results from K–Ar illite fault gouge dating. Nor. Geol. Tidsskr. 96, 275–299. https://doi.org/10.17850/njg96-3-06.

Kylander-Clark, A.R.C.C., Hacker, B.R., Johnson, C.M., Beard, B.L., Mahlen, N.J., Lapen, T.J., 2007. Coupled Lu-Hf and Sm-Nd geochronology constrains prograde and exhumation histories of high- and ultrahigh-pressure eclogites from western Norway. Chem. Geol. 242, 137–154. https://doi.org/10.1016/j.chemgeo.2007.03.006.

Labrousse, L., Jolivet, L., Andersen, T.B., et al., 2004. Pressure-temperature-time deformation history of the exhumation of ultra-high pressure rocks in the Western Gneiss Region, Norway. In: Special Paper of the Geological Society of America, 380, pp. 155–183. https://doi.org/10.1130/0-8137-2380-9.155.

Lacombe, O., 2012. Do fault slip data inversions actually yield " paleostresses" that can be compared with contemporary stresses? A critical discussion. Compt. Rendus Geosci. 344, 159–173. https://doi.org/10.1016/j.crte.2012.01.006.

Larsen, Ø., Fossen, H., Langeland, K., Pedersen, R.B., 2003. Kinematics and timing of polyphase post-Caledonian deformation in the Bergen area, SW Norway. Nor. Geol. Tidsskr. 83, 149–165. https://doi.org/10.1016/j.ajodo.2008.06.033.

Lux, D.R., 1985. K/Ar ages from the Basal Gneiss region, Stadlandet area, western Norway. Nor. Geol. Tidsskr. 65, 277–286.

Mark, D.F., Kelley, S.P., Lee, M.R., Parnell, J., Sherlock, S.C., Brown, D.J., 2008. Ar-Ar dating of authigenic K-feldspar: quantitative modelling of radiogenic argon-loss through subgrain boundary networks. Geochem. Cosmochim. Acta 72, 2695–2710. https://doi.org/10.1016/j.gca.2008.03.018.

Massironi, M., Bistacchi, A., Menegon, L., 2011. Misoriented faults in exhumed metamorphic complexes: rule or exception? Earth Planet Sci. Lett. 307, 233–239. https://doi.org/10.1016/j.epsl.2011.04.041.

Mattila, J., Viola, G., 2014. New constraints on 1.7Gyr of brittle tectonic evolution in southwestern Finland derived from a structural study at the site of a potential nuclear waste repository (Olkiluoto Island). J. Struct. Geol. 67, 50–74. https://doi.org/10.1016/j.jsg.2014.07.003.

Orife, T., Lisle, R.J., 2006. Assessing the statistical significance of palaeostress estimates: simulations using random fault-slips. J. Struct. Geol. 28, 952–956. https://doi.org/10.1016/j.jsg.2006.03.005.

Osmundsen, P.T., Andersen, T.B., 2001. The middle Devonian basins of western Norway: sedimentary response to large-scale transtensional tectonics? Tectonophysics 332, 51–68. https://doi.org/10.1016/S0040-1951(00)00249-3.

Osmundsen, P.T., Andersen, T.B., Markussen, S., Svendby, A.K., 1998. Tectonics and sedimentation in the hangingwall of a major extensional detachment: the Devonian Kvamshesten Basin, western Norway. Basin Res. 10, 213–234. https://doi.org/10.1046/j.1365-2117.1998.00064.x.

Osmundsen, P.T.T., Eide, E.A.A., Haabesland, N.E.E., Roberts, D., Andersen, T.B.B., Kendrick, M., Bingen, B., Braathen, A., Redfield, T.F.F., 2006. Kinematics of the Høybakken detachment zone and the Møre–Trøndelag Fault complex, central Norway. J. Geol. Soc. 163, 303–318. https://doi.org/10.1144/0016-764904-129.

Redfield, T.F., Torsvik, T.H., Andriessen, P.A.M.M., Gabrielsen, R.H., 2004. Mesozoic and Cenozoic tectonics of the Møre Trøndelag Fault Complex, central Norway: constraints from new apatite fission track data. Phys. Chem. Earth 29, 673–682. https://doi.org/10.1016/j.pce.2004.03.005.

Redfield, T.F.F., Osmundsen, P.T.T., Hendriks, B.W.H.W.H., 2005. The role of fault reactivation and growth in the uplift of western Fennoscandia. J. Geol. Soc. 162, 1013–1030. https://doi.org/10.1144/0016-764904-149.

Reeve, M.T., Bell, R.E., Duffy, O.B., Jackson, C.A.L., Sansom, E., 2015. The growth of non-colinear normal fault systems; what can we learn from 3D seismic reflection data? J. Struct. Geol. 70, 141–155. https://doi.org/10.1016/j.jsg.2014.11.007.

Reid-Soukup, D.A., Ulery, A.L., 2018. Smectites. In: Dixon, J.B., Schulze, D.G. (Eds.), Soil Mineralogy with Environmental Applications, pp. 467–499. https://doi.org/10.2136/sssabookser7.c15.

Reiners, P.W., Carlson, R.W., Renne, P.R., Cooper, K.M., Granger, D.E., McLean, N.M., Schoene, B., 2017. Geochronology and Thermochronology. John Wiley & Sons, 2017.

Roberts, A.M., Yielding, G., Kusznir, N.J., Walker, I.M., Dorn- Lopez, D., 1995. Quantitative analysis of triassic extension in the northern Viking Graben. J. Geol. Soc. (Lond.) 152, 15–26. https://doi.org/10.1144/gsjgs.152.1.0015.

Roberts, D., Sturt, B.A., 1980. Caledonian deformation in Norway. J. Geol. Soc. 137, 241–250. https://doi.org/10.1144/gsjgs.137.3.0241.

Røhr, T.S., Bingen, B., Robinson, P., Reddy, S.M., 2013. Geochronology of paleoproterozoic augen gneisses in the western gneiss region, Norway: evidence for Sveconorwegian zircon Neocrystallization and caledonian zircon deformation. J. Geol. 121, 105–128. https://doi.org/10.1086/669229.

Røhr, T.S., Corfu, F., Austrheim, H., Andersen, T.B., 2004. Sveconorwegian U-Pb zircon and monazite ages of granulite-facies rocks, Hisarøya, Gulen, western gneiss region, Norway. Nor. Geol. Tidsskr. 84, 251–256.

Scheiber, T., Fredin, O., Viola, G., Jarna, A., Gasser, D., Łapińska-Viola, R., 2015. Manual extraction of bedrock lineaments from high-resolution LiDAR data: methodological bias and human perception. GFF 137, 362–372. https://doi.org/10.1080/11035897.2015.1085434.

Scheiber, T., Viola, G., 2018. Complex bedrock fracture patterns: a multipronged approach to resolve their evolution in space and time. Tectonics 37, 1030–1062. https://doi.org/10.1002/2017TC004763.

Scheiber, T., Viola, G., Lelij, R. Van Der, Margreth, A., Schönenberger, J., 2019. Microstructurally-constrained versus bulk fault gouge K - Ar dating. J. Struct. Geol. 127, 103868. https://doi.org/10.1016/j.jsg.2019.103868.

Scheiber, T., Viola, G., Wilkinson, C.M., Ganerød, M., Skår, Ø., Gasser, D., 2016. Direct40Ar/39Ar dating of late ordovician and Silurian brittle faulting in the southwestern Norwegian Caledonides. Terra. Nova 28, 374–382. https://doi.org/10.1111/ter.12230.

Seranne, M., 1992. Late Palaeozoic kinematics of the More-Trondelag fault zone and adjacent areas, central Norway. Nor. Geol. Tidsskr. 72, 141–158.

Seranne, M., Seguret, M., 1987. The Devonian basins of western Norway: tectonics and kinematics of an extending crust. Geological Society, London, Special Publications 28, 537–548. https://doi.org/10.1144/GSL.SP.1987.028.01.35.

Simón, J.L., 2019. Forty years of paleostress analysis: has it attained maturity? J. Struct. Geol. 125, 124–133. https://doi.org/10.1016/j.jsg.2018.02.011.

Skyttä, P., Torvela, T., 2018. Brittle reactivation of ductile precursor structures: The role of incomplete structural transposition at a nuclear waste disposal site, Olkiluoto. Finland: J. Struct. Geol. 116, 253–259. https://doi.org/10.1016/j.jsg.2018.06.009.

Steel, R., Ryseth, A., 1990. The Triassic — early Jurassic succession in the northern North Sea: megasequence stratigraphy and intra-Triassic tectonics. Geological Society, London, Special Publications 55, 139–168. https://doi.org/10.1144/GSL.SP.1990.055.01.07.

Talwani, M., Eldholm, O., 1972. Continental margin off Norway: a geophysical study. Geol. Soc. Am. Bull. 83, 3575–3606.

Tartaglia, G., Viola, G., van der Lelij, R., Scheiber, T., Ceccato, A., Schönenberger, J., 2020. Brittle structural facies" analysis: a diagnostic method to unravel and date multiple slip events of long-lived faults. Earth Planet Sci. Lett. 545, 116420. https://doi.org/10.1016/j.epsl.2020.116420.

Theissen-Krah, S., Zastrozhnov, D., Abdelmalak, M.M., Schmid, D.W., Faleide, J.I., Gernigon, L., 2017. Tectonic evolution and extension at the Møre Margin – offshore mid-Norway. Tectonophysics 721, 227–238. https://doi.org/10.1016/j.tecto.2017.09.009.

Torgersen, E., Viola, G., Zwingmann, H., Harris, C., 2015a. Structural and temporal evolution of a reactivated brittle–ductile fault – Part II: timing of fault initiation and reactivation by K–Ar dating of synkinematic illite/muscovite. Earth Planet Sci. Lett. 410, 212–224. https://doi.org/10.1016/j.epsl.2014.09.051.

Torgersen, E., Viola, G., Zwingmann, H., Henderson, I.H.C.C., 2015b. Inclined K-Ar illite age spectra in brittle fault gouges: effects of fault reactivation and wall-rock contamination. Terra. Nova 27, 106–113. https://doi.org/10.1111/ter.12136.

Torsvik, T.H., Andersen, T.B., Eide, E.A., Walderhaug, H.J., 1997. The age and tectonic significance of dolerite dykes in western Norway. J. Geol. Soc. 154, 961–973. https://doi.org/10.1144/gsjgs.154.6.0961.

Torsvik, T.H., Sturt, B.A., Swensson, E., Andersen, T.B., Dewey, J.F., 1992. Palaeomagnetic dating of fault rocks: evidence for Permian and Mesozoic movements and brittle deformation along the extensional Dalsfjord Fault, western Norway. Geophys. J. Int. 109, 565–580. https://doi.org/10.1111/j.1365-246X.1992.tb00118.x.

Viola, G., Scheiber, T., Fredin, O., Zwingmann, H., Margreth, A., Knies, J., 2016. Deconvoluting complex structural histories archived in brittle fault zones. Nat. Commun. 7, 1–10. https://doi.org/10.1038/ncomms13448.

Walsh, E.O., Hacker, B.R., Gans, P.B., Wong, M.S., Andersen, T.B., 2013. Crustal exhumation of the Western Gneiss Region UHP terrane, Norway: 40Ar/39Ar thermochronology and fault-slip analysis. Tectonophysics 608, 1159–1179. https://doi.org/10.1016/j.tecto.2013.06.030.

Wang, C.-C., Wiest, J.D., Jacobs, J., et al., 2021. Tracing the Sveconorwegian orogen into the Caledonides of West Norway: Geochronological and isotopic studies on magmatism and migmatization. Precambrian Res. 362 https://doi.org/10.1016/j.precamres.2021.106301.

Watts, L.M., 2001. The Walls Boundary Fault Zone and the Møre Trøndelag Fault Complex: A Case Study of Two Reactivated Fault Zones. Durham University. http://etheses.dur.ac.uk/3878/.

Weisenberger, T., Bucher, K., 2010. Zeolites in fissures of granites and gneisses of the Central Alps. J. Metamorph. Geol. 28, 825–847. https://doi.org/10.1111/j.1525-1314.2010.00895.x.

Wennberg, O.P., 1996. Superimposed fabrics due to reversal of shear sense: an example from the Bergen Arc Shear Zone, western Norway. J. Struct. Geol. 18, 871–879. https://doi.org/10.1016/0191-8141(96)00014-4.

Wiest, J.D., Jacobs, J., Fossen, H., Ganerød, M., Osmundsen, P.T., 2021. Segmentation of the Caledonian orogenic infrastructure and exhumation of the Western Gneiss Region during transtensional collapse. J. Geol. Soc. 178, jgs2020–j2199. https://doi.org/10.1144/jgs2020-199.

Williams, J.N., Fagereng, Å., Wedmore, L.N.J., Biggs, J., Mphepo, F., Dulanya, Z., Mdala, H., Blenkinsop, T., 2019. How do variably striking faults reactivate during rifting? Insights from southern Malawi. G-cubed 20, 3588–3607. https://doi.org/10.1029/2019GC008219.

Young, D., 2018. Structure of the (ultra)high-pressure Western Gneiss Region, Norway: Imbrication during Caledonian continental margin subduction. Bull. Geol. Soc. Am. 130 (5–6), 926–940. https://doi.org/10.1130/B31764.1.

Zwingmann, H., Mancktelow, N., Antognini, M., Lucchini, R., 2010. Dating of shallow faults: new constraints from the AlpTransit tunnel site (Switzerland). Geology 38, 487–490. https://doi.org/10.1130/G30785.1.